RESEARCH ARTICLE

Special Section:
Magnetism in the Geosciences - Advances and Perspectives

Key Points:
- Keel delamination followed by convective erosion and lithospheric extension can explain the destruction of the eastern North China Craton
- Reactivation of an enriched mantle layer is critical in leading to delamination of cratonic bottom and early postdelamination magmatism
- The heterogeneous lithosphere beneath North China can be produced by postdelamination convective erosion and lithospheric extension

Supporting Information:
- Supporting Information S1
- Figure S1
- Movie S1
- Movie S2
- Movie S3
- Movie S4
- Movie S5
- Movie S6
- Movie S7
- Movie S8
- Movie S9

Correspondence to:
L. Liu, J. P. Morgan, and Y. Xu,
liangliu@gig.ac.cn;
jason.morgan@rhul.ac.uk;
yigangxu@gig.ac.cn

Craton Destruction 2: Evolution of Cratonic Lithosphere After a Rapid Keel Delamination Event

Liang Liu[1,2,3], Jason P. Morgan[2,4], Yigang Xu[1], and Martin Menzies[1,2]

[1]Department of Earth Sciences, Royal Holloway University of London, Egham, UK, [2]State Key Laboratory of Isotope Geochemistry, Guangzhou Institute of Geochemistry, Chinese Academy of Sciences, Guangzhou, China, [3]College of Earth Sciences, University of Chinese Academy of Sciences, Beijing, China, [4]Department of Earth and Planetary Sciences, Harvard University, Cambridge, MA, USA

Abstract Cratonic lithosphere beneath the eastern North China Craton has undergone extensive destruction since early Jurassic times (approximately 190 Ma). This is recorded in its episodic tectonic and magmatic history. In this time, its lithosphere changed thickness from approximately 200 km to <60 km. This change was associated with a peak time (approximately 120 Ma) of lithospheric thinning and magmatism that was linked with high surface heat flow recorded in rift basins. We believe that these records are best explained by a two-stage evolutionary process. First, approximately 100 km of cratonic "keel" underlying a weak midlithospheric discontinuity layer (approximately 80–100 km) was rapidly removed in <10–20 Ma. This keel delamination stage was followed by a protracted (approximately 50–100 Ma) period of convective erosion and/or lithospheric extension that thinned the remaining lithosphere and continuously reworked the former cratonic lithospheric mantle. This study focuses on numerical exploration of the well-recorded second stage of the eastern North China Craton's lithospheric evolution. We find that (1) lithospheric mantle capped by thick crust can be locally replaced by deeper mantle material in 100 Ma due to small-scale convective erosion; (2) asthenospheric upwelling and related extension can replace lithospheric mantle over horizontal length scales of ~50–150 km, and account for observed "mushroom-shaped" low-velocity structures; (3) modeling shows conditions that could lead to the multiple eastern North China Craton magmatic pulses between 190 and 115 Ma that are associated with temporal and spatial changes in magma source petrology and a magmatic hiatus; and (4) a "wet" midlithospheric discontinuity layer provides a potential source material for on-craton magmatism.

1. Introduction

Cratons are generally observed to retain tectonic and magmatic quiescence for billions of years. However, some cratonic regions do record extensive crustal deformation and on-cratonic magmatism that reflect craton destruction processes (Griffin et al., 1998; Menzies & Zhang, 1993). The eastern part of the North China Craton (ENCC) is the best-known Archaean craton to have experienced a recent destruction process (Griffin et al., 1998; Menzies et al., 2007; Menzies & Zhang, 1993; Xu, 2001; Xu et al., 2009; Zhu et al., 2012). Here cratonic lithosphere (approximately 180–220 km; Griffin et al., 1998; Menzies & Zhang, 1993) was thinned to ~60–80 km between early Jurassic and early Cretaceous times (approximately ~190–115 Ma; Xu et al., 2009; Zhu, Jiang, et al., 2012). The process of the ENCC thinning was mainly reflected in the approximately 190–155-Ma "cold" and 135–115-Ma "hot" on-cratonic magmas (Figure 1; Wu et al., 2005; Zhang et al., 2014). Peak ENCC thinning occurred at approximately 120 Ma, and is apparent as widespread crustal melting and formation of metamorphic core complexes (Xu et al., 2009; Zhu et al., 2012; Zhu, Jiang, et al., 2012; Figure 1b), rapid syn-rift surface subsidence, and high heat flow recorded in syn-rift basins (Jiang et al., 2016; Qiu et al., 2016). The modern ENCC lithospheric mantle is a reworked product after craton destruction, and is mainly composed of young asthenosphere-derived lithospheric mantle (Menzies et al., 2007; Xu, 2001; Xu et al., 2009), that still contains preexisting Archean "cratonic" relics (Zhang et al., 2008; Zheng et al., 2001).

We think that this craton's thinning and reworking is best understood as a two-stage evolutionary process. First, approximately 100 km of cratonic keel underlying a weak midlithospheric discontinuity layer (approximately 80–100 km) was rapidly removed in <10–20 Ma. This first stage of "keel delamination" is the focus of a companion paper: *Craton Destruction Part 1: Cratonic Keel Delamination; Liu et al., 2018; which we*
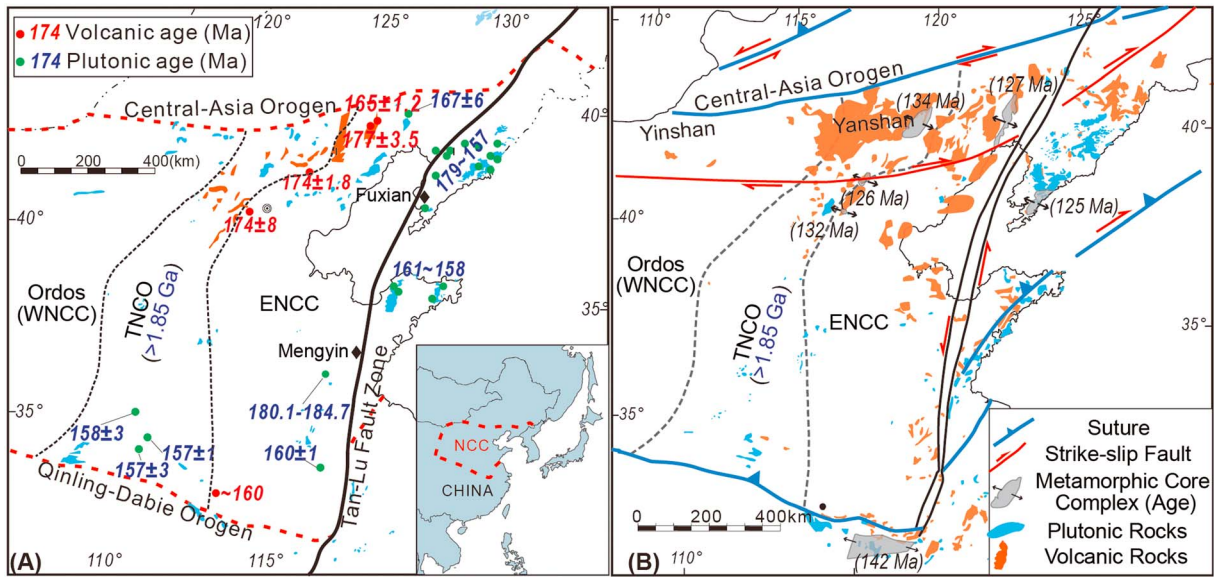
Figure 1. Geological map of the eastern North China craton (ENCC). (a) Distribution of Jurassic magmatism (approximately 190–160 Ma). (b) Distribution of Cretaceous magmatism (approximately 150–100 Ma) and major faults. See details for Cretaceous magma distribution in Figure 11. TNCO = Trans-North China Orogen, WNCC = Western North China Craton.

will hereafter refer to as Part 1. A schematic cartoon of the proposed keel delamination process is shown in Figures 2a and 2b, and a video of a numerical experiment illustrating this delamination stage is shown in Supplementary Video 9. The keel delamination stage was followed by a protracted (approximately 50–100 Ma) period of small-scale convective erosion and/or lithospheric extension that thinned the remaining lithosphere and continuously reworked the former cratonic lithospheric mantle beneath the Moho. The goal of the current study is to better understand this second stage of postkeel-delamination
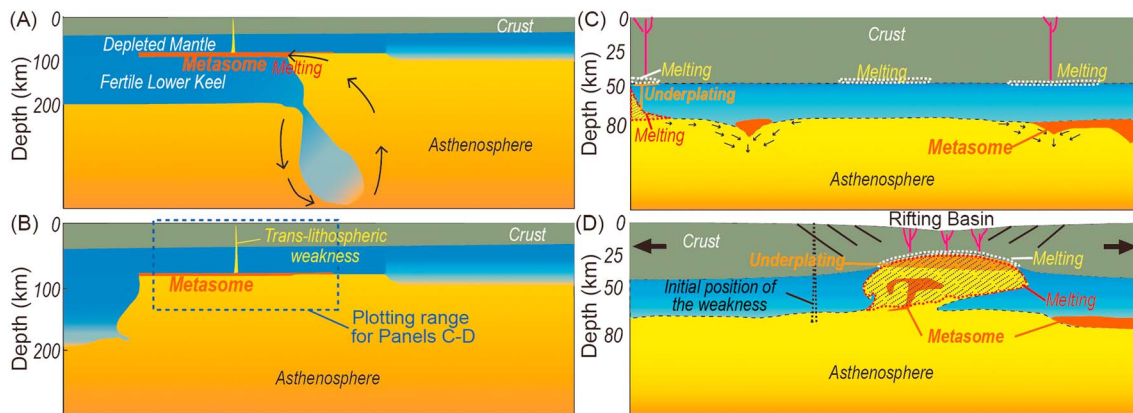

Figure 2. Two-stage craton destruction model. (a and b) Intramantle keel delamination model. (a) An ~10-km weak, partly discontinuous layer (e.g., the metasome midlithosphere discontinuity layer (MLDL)) exists between ~80- and 100-km depths in the craton lithosphere. Because the lower keel is denser than its adjacent asthenosphere and materials adjacent to the edge of metasome are soft enough, the denser lower keel starts to delaminate along the metasome. (The conditions for and evolution of this delamination process are the focus of Part 1; Liu et al., 2018.) (b) Delamination stops where the metasome MLDL disappears. After the delamination of the lower keel, pockets of metasome material locally survive at the base of the lithosphere. The overlying lithosphere initially retains its cool cratonic temperature and does not melt, leading to a magmatic hiatus after initial melting of the metasome warmed by contact with asthenosphere. (c and d) Postdelamination lithospheric evolution. (c) Cold remaining lithosphere can be locally denser than underlying hot asthenosphere. Therefore, dense lithosphere will tend to sag during convective erosion, leading to local thinning of lithosphere and intrusion of asthenosphere and metasome material into the relic cratonic lithosphere. During this process, the remaining lithosphere is slowly heated, and the lower crust can sometimes locally melt. (d) Later lithospheric extension (approximately <140 Ma) can lead to focused magmatism and lithospheric replacement in regions close to preexisting translithospheric weak zone (e.g., the Tan-Lu fault zone).
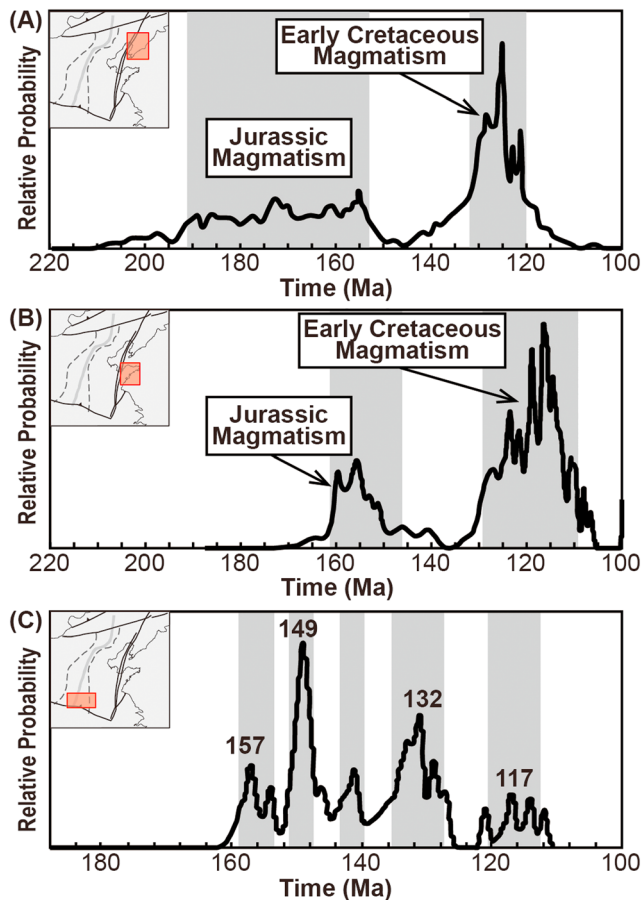
Figure 3. Distribution of magmatic ages in (a) Liaodong (Wu et al., 2005), (b) Jiaodong (Zhang et al., 2014), and (c) Xiaoqinling (Zhang et al., 2014). On-craton magmatism occurred earlier in the northern ENCC (~190 Ma) than in the southern ENCC (~160 Ma). An ~10–20-Ma magmatic hiatus is always recorded on the ENCC after the Jurassic magmatic pulse. Regions in (a) and (b) experienced at least two magmatic pulses after the earliest Jurassic pulse(s), although magmatism can be locally continuous.

evolution of relic ENCC crust and uppermost lithospheric mantle. Our primary tool to do this will be to explore and compare the implications of a suite of numerical experiments with observed patterns of post-Jurassic magmatism and deformation in the ENCC. Before diving into the numerical experiments and their ability to match the ENCC's well-documented postdelamination history, we first summarize the petrological, geochemical, geological, and geophysical observations that have been used to constrain the ENCC's recent evolution.

2. Tectonic and Magmatic Evolution During ENCC Destruction

The ENCC destruction process is reflected in its episodic tectonic and magmatic (felsic-magma-dominated) record. Due to its location adjacent to active subduction-collision zones, a primarily compressional state of the ENCC appeared no later than approximately 320 Ma (Meng, 2003; Xu et al., 2009). During this time, the crust along its margins is proposed to be locally thickened to approximately 50 km (cf. Meng, 2003). (Alternatively, it is also possible that these crustal regions were initially thickened during the Archaean (Kinck et al., 1993; Youssof et al., 2013; Zhai & Santosh, 2011).) Locally, lithospheric extension initiated at approximately 160–155 Ma, recorded in the subsidence of rift basins (He & Wang, 2004; Meng, 2003). On the inner craton, the tectonic state generally transformed to be extensional at the Early Cretaceous times (approximately 140 Ma; Figure 1b; Meng, 2003), which is suggested to be related to the change in subduction directions of the paleo-Pacific plates (Xu et al., 2009; Zhu, Jiang, et al., 2012).

Between approximately 190 and 160 Ma, magmatism moved from the margin to the interior (Figure 1). By approximately 160 Ma, the ENCC keel appears to have been thinned to approximately 100–80 km, the depth range of the commonly observed midlithosphere discontinuity (MLD; Selway et al., 2015). Contact of the MLD layer (or MLDL) with hot, newly infilled asthenosphere triggered melting of this water-rich metasomatic layer known petrologically as the "metasome," which is believed to be composed of mica-amphibole-rutile-ilmenite-diopside (Menzies & Zhang, 1993; Xu, 2001).

After a magmatic hiatus lasting 10–20 Ma, a second episode of magmatism occurred between approximately 150 and 115 Ma (Figure 3; Xu et al., 2009; Zhang et al., 2014; Zhu, Jiang, et al., 2012). Locally, the pattern of magmatism can vary; for example, multiple magmatic pulses are identified without any magmatic hiatus on the southwestern ENCC (Figure 3c). Most of these magmas had stagnated close to the ENCC's convergent margin (Figure 1) that used to be capped by >50-km-thick crust (Meng, 2003; Xu et al., 2009) and the localized lithosphere-scale Tan-Lu fault zone (Menzies et al., 2007; Zhu et al., 2010). In previous studies, this 190–115-Ma on-cratonic magmatism is proposed to reveal a long-lasting process of the craton destruction (Menzies et al., 2007; Xu, 2001; Xu et al., 2009; Zhu, Jiang, et al., 2012).

By the end of the second episode (approximately 100 Ma), the ENCC lithospheric mantle had been replaced largely by asthenosphere-derived material with little xenolithic evidence for cratonic relics (Menzies et al., 2007; Xu, 2001). Mantle replacement beneath the Moho is supported by the high heat flow recorded in sedimentary basins (~90–100 W/m^2; Qiu et al., 2016). The ENCC lithospheric thinning or mantle replacement rate appears to have been "slow," e.g., ~0.3 km/Ma, assuming that ~80 km at 160 Ma changed to ~60 km at 100 Ma.

The modern ENCC mantle appears to be heterogeneous in terms of its isotopic age and seismic velocity (Figure 4). The mantle xenoliths entrained in <80-Ma basalts generally indicate a young and asthenospheric derived feature for the ENCC mantle (Hong et al., 2012; Xu, 2001; Xu et al., 2009), but ancient mantle
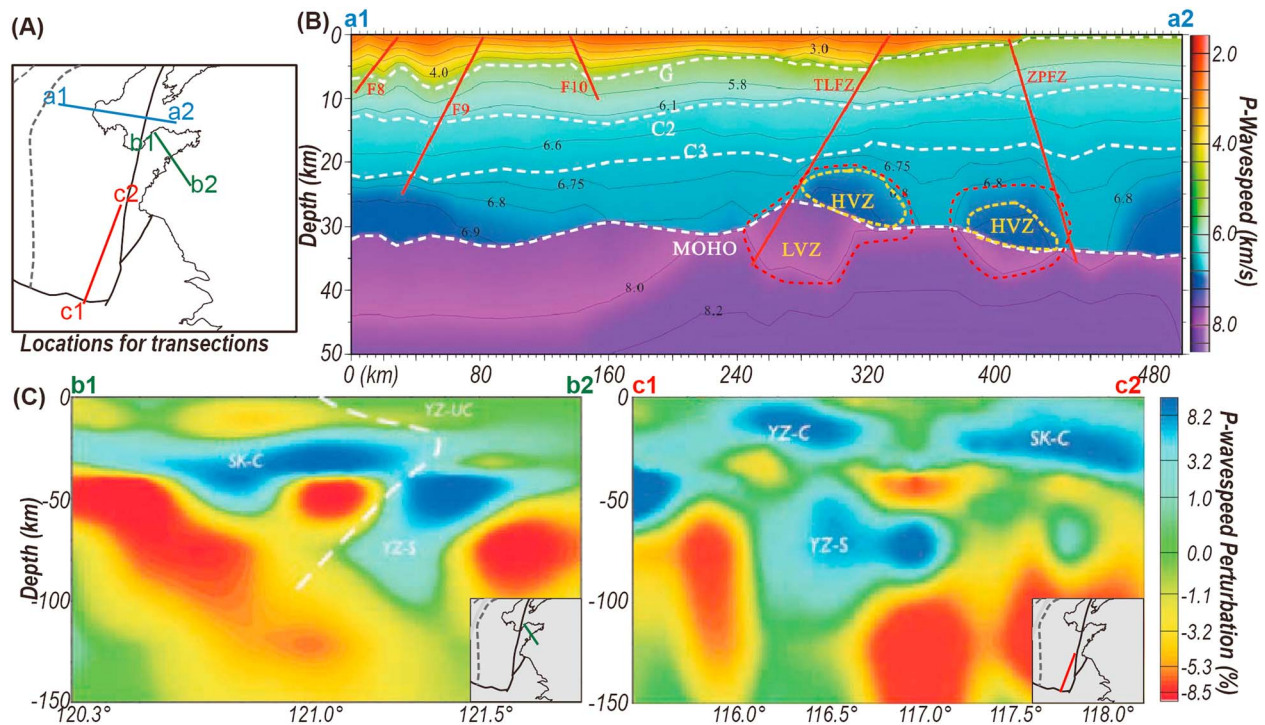
Figure 4. (a) Locations for seismic transects in (b)–(d). (b) Refraction profile along the a1 and a2 transect in (a; Hao et al., 2013). Regions contoured by red dashed lines are the seismic wave speed "mushroom" structures that we think are associated with asthenosphere intruding into extending lithosphere (see text for more details). TLFZ = Tan-Lu fault zone, ZPFZ = Zhangjiakou-Penglai fault zone, HVZ = high-velocity zone, LVZ = low-velocity zone. F8, F9, and F10 represent small-scale faults (see more details in Hao et al., 2013). (c and d) Seismic tomography structure along the b1-b2 and c1-c2 transects in (a; Xu et al., 2002).

components do also locally exist (Zhang et al., 2008; Zheng et al., 2001). Seismic tomography reveals a 50–150-km-wide mushroom-like low-velocity anomalies within the lithospheric mantle, especially close to the Tan-Lu fault zone, and these "mushrooms" are underlain by high-velocity anomalies within the crust (Hao et al., 2013; Xu et al., 2002; Yuan, 1996).

These features are taken as the most important basis by geologists for reconstructing the process of the ENCC destruction (Menzies et al., 2007; Xu, 2001; Xu et al., 2009; Zhu, Jiang, et al., 2012). However, the requirement for both "fast" and slow aspects to the destruction of the craton, the origin and distribution of the on-cratonic magmas, and the origin of the heterogeneous modern ENCC mantle have not been addressed in previous numerical modeling studies:

1. A "rapid" magmatic flare-up has been linked to many processes including lithospheric delamination along the weak and/or deep Moho (Bird, 1979; Gao et al., 2004; Kay & Kay, 1993), Rayleigh–Taylor type gravity instability (Gorczyk et al., 2012; Harig et al., 2010), and lithospheric rifting (Liao & Gerya, 2014; Lin et al., 2005; Wenker & Beaumont, 2017).
2. Mechanisms used to explain on-craton magmatism include convective erosion (cf. Conrad & Molnar, 1997), assuming that cratonic keel lost its high strength before thinning, due to long-term (>1 Ga) mantle refertilization, or short-term (<200 Ma) in situ metasomatism-related mantle transformation linked to dehydration in underlying (paleo-) Pacific slabs (He, 2014; Liao et al., 2017; Niu, 2005; Wang et al., 2016; Xu, 2001; Yang et al., 2017; Zhang et al., 2008).

We infer from the above observations that a two-stage process led to craton reworking in the ENCC (Liu et al., 2016). First, over a period of 10–20 Ma, approximately 100 km of the cratonic keel was rapidly removed along a weak midlithospheric discontinuity layer (MLDL) that may have had a composition similar to the proposed metasome (Karato et al., 2015; Menzies & Zhang, 1993; Selway et al., 2015; Xu, 2001). We propose that this happened during a discrete keel delamination event (see Figures 2a and 2b and Supplementary Video 9), with a detailed investigation of this process in the companion paper (Liu et al.,

2018). Second, the remaining cratonic lithospheric mantle was progressively replaced by asthenospheric mantle during convective erosion associated with widely spread localized lithospheric extension along preexisting fault(s).

This paper focuses on the postdelamination process (stage 2). There have been many conceptual models for craton destruction, many with contradictory assumptions and conclusions. To guide our investigation, we aim to keep the following issues in mind:

1. When (and why) does melting occur in the crust?
2. Do translithospheric weaknesses have an important role to play in craton failure?
3. What is the role, if any, for "in situ" metasome-linked water?

3. 2-D Numerical Methods

3.1. Thermomechanical Code

A 2-D incompressible Lagrangian finite element code with a free surface boundary condition is used for the numerical experiments (Andrés-Martínez et al., 2015; Hasenclever, 2010; Hasenclever et al., 2011). Crust and mantle are assumed to be incompressible elastoviscoplastic materials that deform by both Newtonian and non-Newtonian creep. Material melting is found using methods described in Hasenclever (2010) and Morgan (2001). Tracer particles are added for tracking different material properties. The 2-D experimental domain is subdivided using an adaptive triangle mesh generator that tracks material boundaries and interfaces, for example, between asthenosphere and lithospheric mantle. A Drucker-Prager yield criterion is added to evaluate and formulate plasticity in extension experiments (cf. Moresi et al., 2003). More details on the numerical approach are given in Andrés-Martínez et al. (2015), Hasenclever (2010), Hasenclever et al. (2011), the attached appendices, and those in Part 1 (Liu et al., 2018). Table 1 shows the parameters used in numerical experiments. Table 2 summarizes the major variables tested in numerical runs.

3.2. Model Setup

3.2.1. Initial Material Layering and Material Conditions

The initial lithosphere thickness is at 90 km, which contains a basal 10-km MLDL. This initial condition reflects the postkeel-delamination state of the ENCC lithosphere following a keel delamination event beneath a weak, buoyant metasoma-layer-like MLDL. The crustal thickness in runs 1–4 and 9–11 is set at 40 km to be the initial value beneath inner cratonic areas (cf. Xia et al., 2017). To investigate the effect of increased crustal thickness on magmatism in the ENCC's compressionally thickened margins (Figure 1b), the crustal thickness chosen in runs 5–8 and 12–15 is 50 km. An ~50-km crustal thickness appears to still remain beneath parts of the ENCC and the western North China Craton (e.g., beneath the southwestern ENCC and the western Ordos Basin; Chen et al., 2014; Xia et al., 2017).

To study the potential effects of preexisting lithospheric fault zones in controlling lithospheric evolution and magmatic distribution (cf. Deng et al., 2013; Menzies et al., 2007; Yuan, 1996), in runs 9–15, a 5-km-wide zone of asthenospheric material is placed in the middle of the modeling box at ranges between 90 and 60 km, to act as an initial weak zone in the lithosphere. Vertical weak zones have been reported beneath some fault zones (cf. Pollitz et al., 2001). In the case of the ENCC, they could possibly be created by long-term-active lithospheric shearing close to the Tan-Lu fault (Zhu et al., 2010).

3.2.2. Material Densities

The MLDL material is assumed to have a compositional density identical to that of MARID mantle xenoliths (Dawson & Smith, 1977). Given that "margin processes" might reduce the compositional density ρ_{co} of the mantle wedge (Gerya et al., 2006), while Fe-rich mafic melts could also increase the ρ_{co} of the overlying lithospheric mantle (Griffin et al., 2009; Zhang et al., 2008), the ρ_{co} difference between lithospheric mantle material and asthenosphere is varied in runs 1–8 (Figures 5d–5f). These experiments will allow us to study the potential effects of more or less compositionally buoyant asthenosphere on convective erosion of the lithosphere.

3.2.3. Melting Parameters

Bimodal patterns of magmatism are an important feature of the postdelamination history of the ENCC. These models also allow us to explore potential magmatism associated with metasome heating by

Table 1
Parameters for the Numerical Experiments Discussed in the Paper

Parameters	A.M.	Metasome	D.M.	L.C.	M.C.	U.C.
Flow Law Parameters[1–7]						
A_{dis} (Pa^{-n}·s^{-1})	$10^{-15.05}$	$10^{-15.05}$	$10^{-15.56}$	$10^{-21.05}$	$10^{-15.4}$	10^{-28}
n_{dis}		3.5		4.2	3.0	4.0
E_{dis} (kJ/mol)	480	480	530	445	356	223
V_{dis} (cm^3/mol)		8			—	
A_{dif} (Pa^{-n}·s^{-1})		$10^{-8.65}$		$10^{-13.3}$	$10^{-13.3}$	$10^{-8.4}$
n_{dif}			1			
E_{dif} (kJ/mol)	335	335	375	170	170	220
V_{dif} (cm^3/mol)		4			—	
r		r_{dif}=1.93, r_{dis}=1.95			—	
Elasticity and Plasticity[7]						
G (GPa)		74		40	40	36
C_0 (Mpa)			20			
Φ (°)			30 ($\gamma = 0$) →15 ($\gamma > 1.5$)			
Thermal Parameters[7–9]						
k (Wm^{-1}K^{-1})		3.3		2.5	2.5	2.1
H_r (μW/m^3)		0.033		0.25	0.25	1
c_p (J/(kg·K))			1200			
T_0^m (°C)	1081	1081	1136		—	
$(\partial T^m/\partial f)_p$		132			—	
$(\partial T^m/\partial P)_f$		250			—	
Q_L (kJ/kg)		400			—	
Density Parameters[10–11]						
ρ_0 (g·cm^{-3})	—	3.32	3.31	2.85	2.85	2.7
a_1 (10^{-4})	0.2697	0.2697	0.27165		0.27014	
a_2 (10^{-8} K^{-1})	1.0192	1.0192	1.04971		1.05945	
a_3 (K^2)	−0.1282	−0.1282	−0.15031		−0.1243	
K (Gpa^{-1})	134	134	129		63	

Note. Dislocation and diffusion viscosities are determined as $\eta = 1/2A^{-1/n}C_{OH}^{-r/n}\varepsilon_{II}^{1/n-1}\exp((E + P \cdot V)/nRT)$, where η is the viscosity, ε is the second invariant of strain rate, A is a preexponential constant, E is the activation energy, C_{OH} is the water content in ppm H/Si (for olivine Fo90: 1 ppm (wt) H_2O = 16.35H/10^{6}Si), r describes the exponential dependency on water, R is the universal gas constant, T is the temperature, P is the pressure, and V is the activation volume. Subscript *dis* refers to parameters for dislocation creep, while *dif* is for diffusion creep.
Parameter references: (1) Hirth & Kohlstedt (2004), (2) Wilks & Carter (1990), (3) Rybacki & Dresen (2004), (4) Gleason & Tullis (1995), (5) Rutter & Brodie (2004), (7) Brune et al. (2014), (8) Morgan (2001), (9) Korenaga & Karato (2008), (10) Djomani et al. (2001), and (11) Schutt & Lesher (2006).
Other symbols: G = shear modulus, C_0 = cohesion, Φ = friction angle, k = thermal conductivity, H_r = radioactive heat production, c_p = heat capacity, T_0^m = solidus at room temperature and pressure, $(\partial T^m/\partial f)_p$ = solidus's dependence on degree of melt extraction, $(\partial T^m/\partial P)_f$ = solidus's dependence on pressure, Q_L = latent heat, ρ_0 = reference density at room temperature (20 °C) and pressure (0.1 MPa), K = bulk modulus.
Abbreviations: A.M. = asthenosphere, D.M. = depleted mantle, L.C. = lower crust, M.C. = middle crust, U.C. = upper crust.

newly infilled asthenosphere, melting associated with asthenospheric infilling and reworking of the relic ENCC lithosphere and crust, and crustal melting associated with its potential reheating. In these experiments, the asthenosphere is assumed to contain 100 ppm water as has been estimated for oceanic basalt sources (cf. Hirschmann et al., 2005). In contrast, MLDL material is assumed to contain 1000 ppm water (cf. Karato et al., 2015). No initial depletion is assumed for upper and middle crusts, and we treat their melting behavior to be that of amphibolite (cf. López & Castro, 2001; Figure A1a). A 20% initial depletion is used for lower crustal material to simulate the preexistence of granulite-facies rocks (Gao et al., 1998), whose petrology can be treated as the residue after ~20% melt extraction from an amphibolite (cf. Rapp & Watson, 1995). See the Appendix for the mantle and crustal solidi used in the numerical experiments.

3.2.4. Initial and Boundary Conditions

For the initial temperature field, a 1-D steady state conductive thermal profile (Turcotte & Schubert, 2014) for "stable" 200-km lithosphere (with various initial crustal thicknesses; Figure 5b and Table 2) is used for the uppermost lithospheric layers. Below the MLDL, the starting temperature of asthenosphere is set to be

Table 2
Variables in Each Run

Convective erosion modeling (extension speed = 0)			
40-km-crust scenario			
Run no.	Run 1	Run 2	Run 3	Run 4
$\rho_{A.M.}\vert\rho_{L.M.}$ (kg/m^3)	3360|3310	3340|3310	3320|3310	3300|3310
50-km-crust scenario			
Run no.	Run 5	Run 6	Run 7	Run 8
$\rho_{A.M.}\vert\rho_{L.M.}$ (kg/m^3)	3360|3310	3340|3310	3320|3310	3300|3310
Lithospheric extension modeling ($\rho_{A.M.}\vert\rho_{L.M.}$ = 3360|3310 kg/m^3)			
40-km-crust scenario			
Run no.	Run 9	Run 10	Run 11	
Extension speed	1 mm/year	2 mm/year	3 mm/year	
50-km-crust scenario			
Run no.	Run 12	Run 13	Run 14	Run 15
Extension speed	1 mm/year	2 mm/year	3 mm/year	4 mm/year

Note. $\rho_{A.M.}$ = compositional density of asthenosphere, $\rho_{L.M.}$ = compositional density of lithospheric mantle.

1350 °C to simulate the situation just after the rapid influx of warm asthenosphere during a rapid delamination event. The surface boundary is fixed at 0 °C. The bottom boundary is fixed to be that of the asthenospheric potential temperature (1350 °C).

The following experiments will be presented in two groups. In runs 1–8, no effects of extension are considered; while the effects of extension are studied in runs 9–15. For runs without extension (runs 1–8), a free slip boundary condition is used for the left, right, and bottom boundaries. For runs with extension (runs 9–15), an outward speed (Table 2) is imposed along the right-hand side of the computational region for 50 Ma to simulate the maximum extension duration on the ENCC as discussed above, while the lower boundary of the region has an upward velocity taken to ensure overall material balance,

$$v_{vertical} = v_{right} L_{bottom} / L_{right} \tag{1}$$

where v_{right} is the speed prescribed along the right boundary (ranging from 1 to 4 mm/year), $v_{vertical}$ is the speed prescribed along the bottom boundary, L_{right} is the evolving length of the right boundary, and L_{bottom} is the evolving length of the bottom boundary.

4. Results

For comparison with the above geological and geophysical observations on the ENCC (section 2), the following experimental results will be discussed in terms of their melting behavior and lithospheric reworking/replacement. A summary of results will be presented before describing the specific processes of convective erosion or lithospheric extension. Experiments without lithospheric extension will be presented before those with extension.

4.1. Experimental Goals and Variables
4.1.1. Goal and Variables Studied With Extension-Free Experiments

Prior to lithospheric extension, on-cratonic magmatism appears to have been focused close to the ENCC's margins. This may have happened because these regions had initially thicker crust and/or a special sub-duction margin density structure discussed in previous studies (e.g., Gerya & Yuen, 2003; Hasenclever et al., 2011; Gerya & Yuen, 2003; Xu et al., 2009). In runs 1–8, both factors are variables to be explored.

To study potential effects of thicker crust, a 50-km-thick crust is set in runs 5–8, which have a hotter initial geotherm (Figure 5b); for comparison, the crustal thickness is set at 40 km in runs 1–4, possible as a predestruction value for the inner craton (cf. Xia et al., 2017).
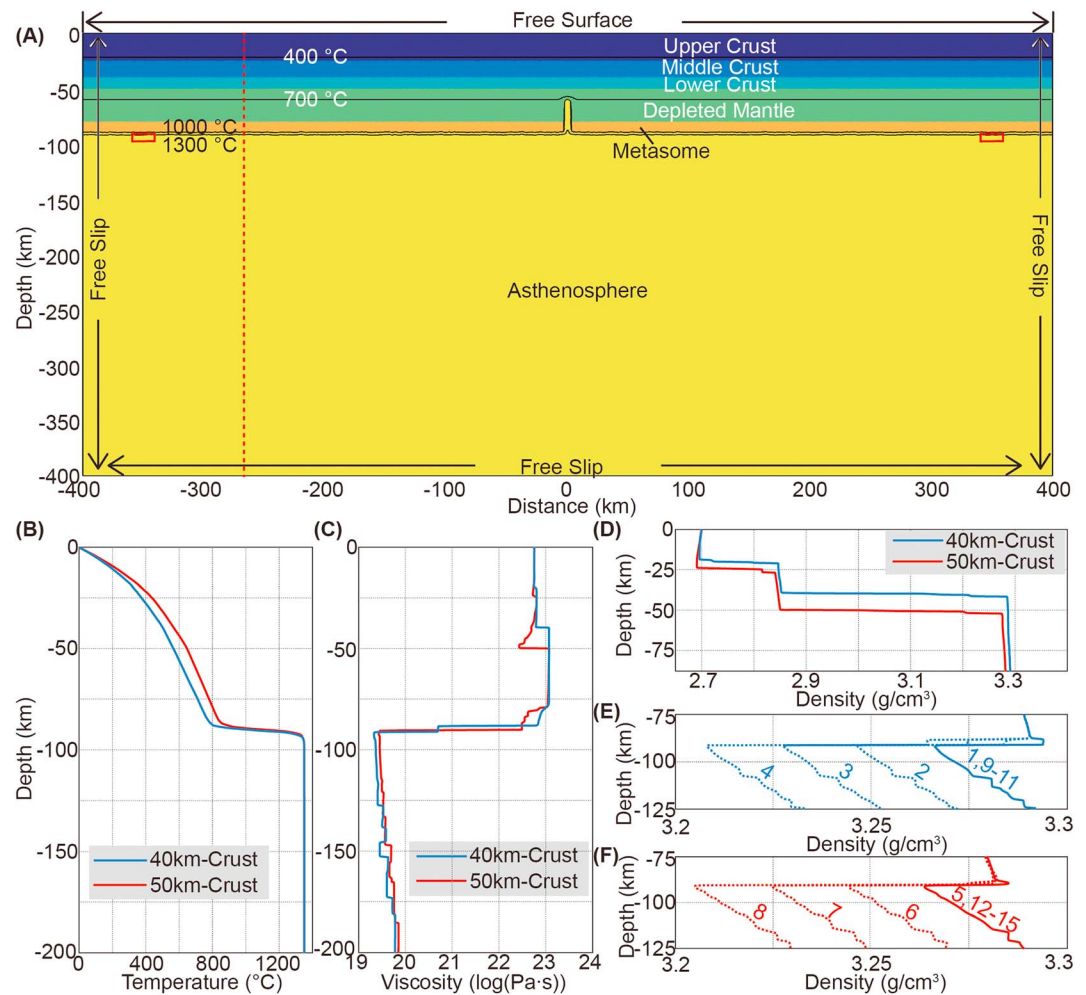
Figure 5. Model setup. (a) The postdelamination ENCC lithosphere is assumed to be 90 km thick, containing, from its top to bottom, 50-km-thick (margin) or 40-km-thick crust (interior), lithospheric mantle containing a basal metasome (10 km) within 40–50-km-thick relic cratonic (depleted) mantle that lies above the metasome layer. A ~5-km-wide zone of asthenosphere-like material is added between 90- and 60-km depths at the center to simulate an initial lithospheric weak zone. To trigger small-scale mantle convection in runs 1–8, two 20-km-wide × 10-km-thick dense (3.4 g/cm³) blocks (see small red rectangles) are set at −350 and 350 km, close to the left and right boundary segments. These two blocks sink to the bottom within 0.5 Ma and do not obviously affect the experiment following their initial sinking. The mesh resolution (~2 km) close to phase boundaries (~20 km) is approximately 10 times finer than in regions far away (~95 km) from phase boundaries. (b) The initial temperature profile of numerical experiments is the red dashed line in (a). Forty-kilometer-crust scenarios include runs 1–4 and runs 9–11; 50-km-crust scenarios include runs 5–8 and runs 12–15 (also see Table 2). (c) Initial viscosity profile of numerical experiments. (d) Initial density profile of numerical experiments above 80-km depth. (e) The 75–125-km depth range is zoomed up to demonstrate the initial density structure in runs 1–4 and 9–11. (f) A similar amplification is also made for the initial density structure of runs 5–8 and 12–15. In (e) and (f), numbers beside the density profile represent the run numbers of the numerical experiments considered here.

Given that "margin processes" might reduce the compositional density ρ_{co} of the mantle wedge (Gerya & Yuen, 2003), while associated Fe-rich mafic melts could also enhance the ρ_{co} of the overlying depleted lithospheric mantle (Griffin et al., 2009; Zhang et al., 2008), the ρ_{co} difference ($\Delta\rho_{co}$) between lithospheric mantle (ρ_{co}^{L}) and asthenosphere (ρ_{co}^{A}) is varied in runs 1–8 (Figures 5d–5f and Table 2).

4.1.2. Goals and Variables Studied in Experiments With Net Lithospheric Extension

In regions close the Tan-Lu fault zone, presently far from convergent margins, the observed enhanced magmatism and mantle heterogeneity may have been shaped by variable extension and/or crustal thickness (40 km thick for runs 9–11 and 50 km thick for runs 12–15; Table 2). In runs 9–15, the crustal thickness and the rate of lithospheric extension are considered as variables in each experiment.
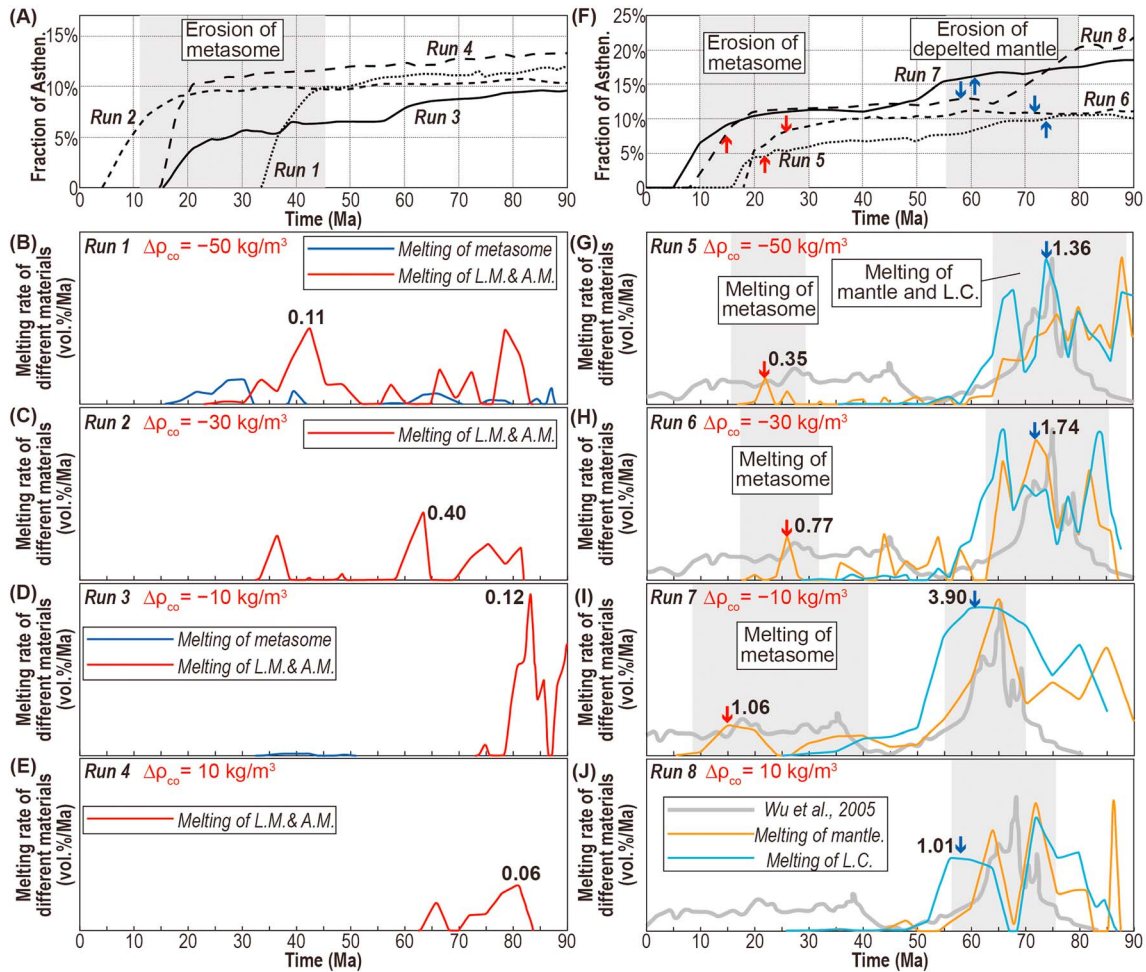
Figure 6. Results of experimental runs without lithospheric extension. (a–e) Runs 1–4 with 40-km-thick crust. (a) Fraction of asthenosphere material within reworked lithosphere above 90-km depths. By the end of these experiments, asthenosphere material has replaced ~10–15% of the original relic cratonic lithosphere. Asthenosphere replacement of this initial metasoma layer accounts for ~10% of the intruded material, while replacement of depleted cratonic mantle accounts for <5%. (b–e) Melting rates of different materials (in volume proportion per million years) above 100-km depths. (f–j) Runs 5–8 with 50-km-thick crust. (f) Fraction of asthenosphere material within reworked lithosphere above 90-km depths. By the end of these experiments, asthenosphere has replaced ~10–25% of the relic cratonic lithosphere. Replacement of initial metasome MLDL material accounts for ~10% and replacement of relic cratonic mantle accounts for <15%. (g–j) Melting rates of different materials (in volume proportion per million years) at depths shallower than 100 km. The thick gray line is from Figure 3a. Labels for lines in (g)–(i) are same as those in (j). The horizontal range is between −400 and 0 km (Figure 5a). L.C. = lower crust, L.M. = lithospheric mantle, A.M. = asthenospheric mantle, $\Delta\rho_{co}$ = the compositional density difference between lithospheric mantle and asthenosphere.

4.2. Experiments Without Lithospheric Extension

Runs 1–8 are designed to investigate the evolution of the relic keel without regional postdelamination extension. In these runs, convective erosion leads to lithospheric reworking/replacement and introduces ~10–> 20% asthenosphere into the reworked lithosphere (Figures 6a and 6f). Minor melting occurs in the runs with 40-km-thick crust (Figures 6b–6e), and two melting pulses are generally observed in those with 50-km-thick crust (Figures 6f–6j).

In runs 1–4 with 40-km-thick crust, ~10% lithosphere is replaced by asthenosphere after 100 Ma and minor melting of mantle occurs at ~20 Ma after the lithospheric is heated up (Figures 6a–6e). In these runs, increasing the compositional density difference ($\Delta\rho_{co} = \rho_{co}^L - \rho_{co}^A$) does not affect the results.

In runs 5–8 with 50-km-thick crust, two pulses of melting are observed (Figures 6g–6j). The first pulse is minor, caused by metasome melting. The second pulse features both mantle and lower crustal melting, dominated
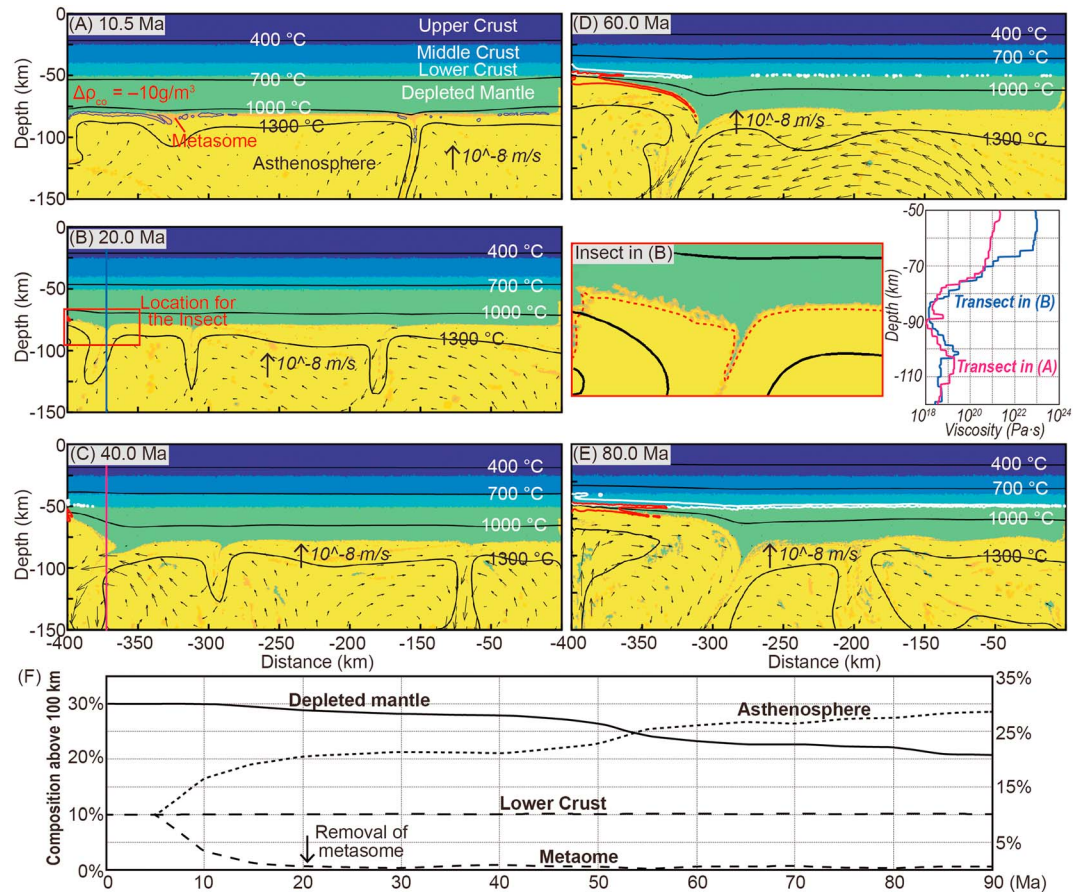
Figure 7. Convective erosion of relic lithosphere (run 7). (a) Due to the weak rheology of the metasome MLDL material, it joins into small-scale convection after being heated. Metasome melting marks the first melting pulse at ~10–20 Ma. (b) Due to its higher net density (Figure 5f), during small-scale convection, the depleted mantle entrains into the downwelling asthenosphere in the form of small drops. These sinking drops pull adjacent materials toward the locus of sinking. The overall process leads to local lithospheric thinning (or asthenospheric diapirs; see the insect). A small melting region appears within the asthenospheric diapir. (c) The continuous growth of cratonic lithospheric drops results in a larger horizontal temperature variation and accelerates the small-scale convection. When an asthenospheric diapir impends near the crust, lower crust melting occurs. (d) Asthenosphere contacts with lower crust, as the mantle melting depth range expands continuously. (e) Approximately 30% of reworked old lithosphere has been replaced by asthenosphere. (f) Volume fractions of different materials above 100-km depth. In (a)–(e), white lines mark contours of crustal melt extraction, red lines mark contours of mantle melt extraction (with depletion >5%), and blue contours in (a) show metasome melt extraction. $\Delta\rho_{co}$ = the compositional density difference between lithospheric mantle and asthenosphere.

by crustal melting. The rate of lithosphere replacement increases to >20% only when $\Delta\rho_{co} < -10$ kg/m^3 (Figure 6b). Runs 8 and 4 consider a less likely scenario, as the compositional density (3.31 g/cm^3 at STP condition) of depleted mantle is generally thought to be less than that of the asthenosphere (3.36–3.39 g/cm^3 at STP condition; cf. Djomani et al., 2001).

4.2.1. Convective-Erosion-Dominated Lithospheric Reworking

Run 7 is taken as a type example to describe convective erosion of the lithosphere in absence of extension.

Most of the metasome material enters small-scale mantle convection in the form of small drops and mix with asthenosphere after the start of experiment (i.e. 20 Ma; Figures 7a and 7f). This is due to the fact that the metasome has a weak rheology and a locally greater density (Table 1). Its high-water content (~1,000 ppm) is associated with a low solidus, which means that metasome melting dominates the early melting pattern (i.e., 20–10 Ma, Figure 6i).
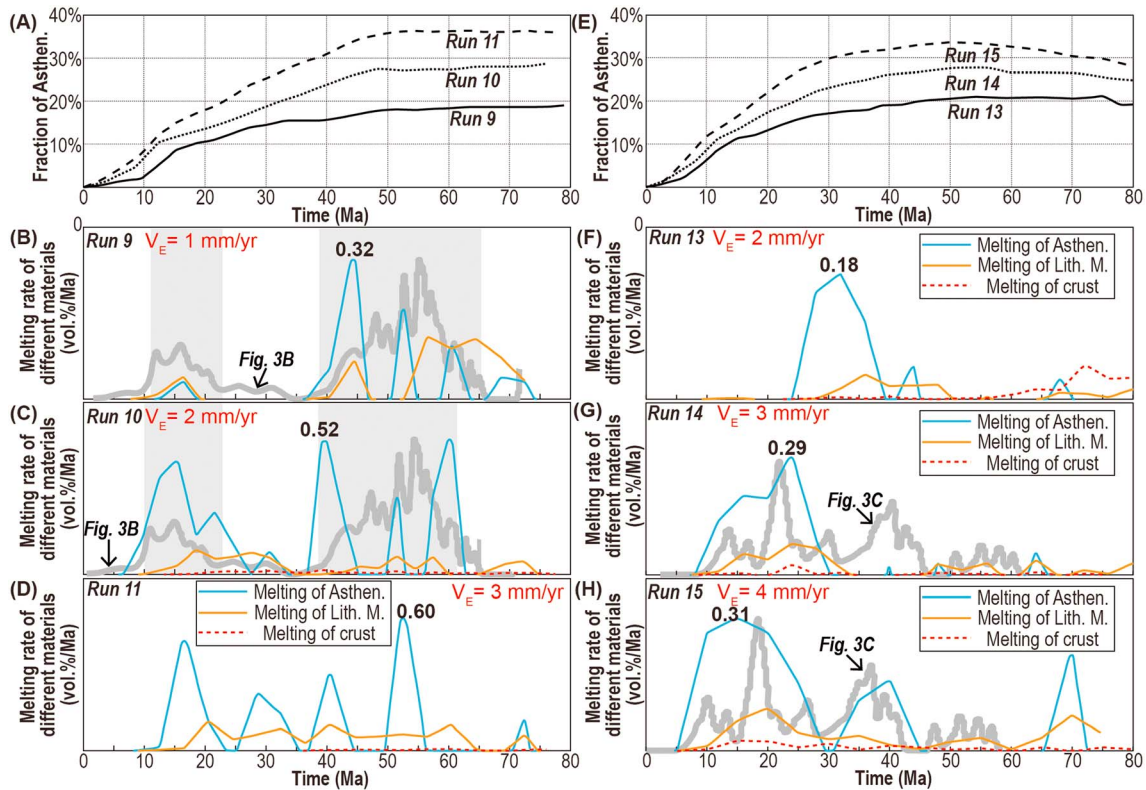
Figure 8. Results of experimental runs with lithospheric extension (close to the extensional locus). (a–d) Runs 9–11 with 40-km-thick crust. (a) Fraction of asthenosphere above 90-km depth. (b–d) Melting rates of different materials (in volume proportion per million years) above 100-km depth. The thick gray line is from Figure 3b. Labels for lines in (b) and (c) are same as those in (d). (e–h) Runs 13–15 with 50-km-thick crust. (e) Fraction of asthenosphere above 90-km depth. (f–h) Melting rates of different materials (in volume proportion per million years) above 100-km depth. The thick gray line is from Figure 3c. The horizontal plotting range is between −150 and 250 km (see Figure 5a). Lith. M. = lithospheric mantle, Asthen. = asthenosphere, V_E = extension rate.

Thereafter, depleted cratonic mantle is in direct contact with the hotter underlying asthenosphere. Lithospheric downwelling stretches the surrounding materials so that lithosphere close to the sinking center thins and small asthenospheric diapirs begin to form (Figure 7b). The initial diapirs are small (<15 km) and occur close to the ends/edges of the stretching depleted mantle region. Lower crustal melting begins above the asthenospheric diapirs, and initial pressure-release mantle melting occurs in the top of the asthenospheric diapirs (Figure 7b).

Asthenospheric diapirs and melting regions gradually grow wider as the sinking center moves toward the inner lithosphere. In this way, ~20% lithosphere is replaced by asthenosphere (i.e., 80 Ma; Figures 7e and 7f). The newly accreted materials (asthenospheric + metasome + lithosphere) cool to a stage where the 1300 °C potential contour appears at >80-km depth (Figure 7e).

4.3. Experiments With Lithospheric Extension

Runs 9–15 are designed to investigate the evolution of relic keel under an extensional scenario. Lithospheric extension leads to ~50–150-km-wide lithosphere to be replaced by "mushroom"-like upwelling materials. Two pulses of melting occur in the runs with 40-km-thick crust (Figures 8b, 8c, and 9b–9d), while the melting behavior in the runs with 50-km-thick crust appears to be continuous without obvious hiatuses (Figures 8g, 8h, and 9f–9h). In comparison to scenarios without extension, crustal melting is rare and is not observed in regions away from the center of extension (Figure 9).

The initial crustal thickness does not obviously affect the general pattern of lithospheric replacement. Approximately 50–150-km-wide lithosphere is replaced by a mushroom-shaped upwelling composed of metasome and/or asthenospheric materials.
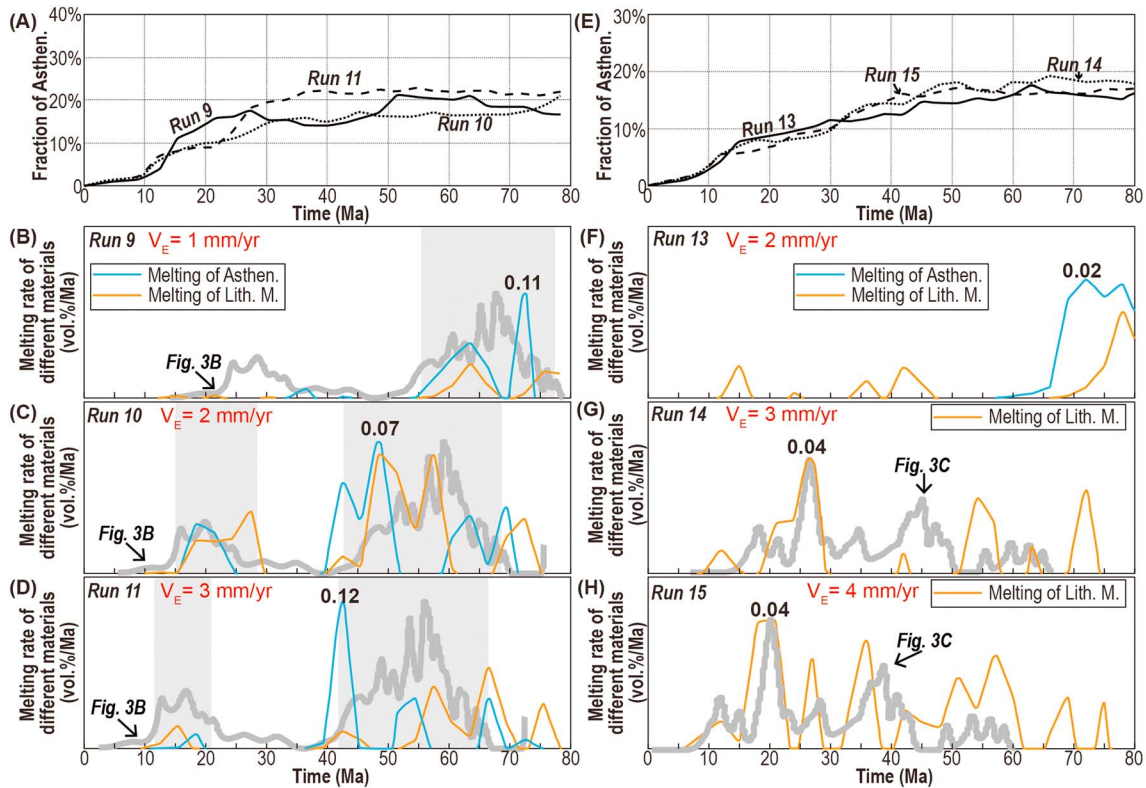
Figure 9. Results of experimental runs with lithospheric extension (away from the extensional locus). (a–d) Runs 9–11 with 40-km-thick crust. (a) Fraction of asthenosphere above 90-km depth. (b–d) Melting rates of different materials (in volume proportion per million years) above 100-km depth. The thick gray line is from Figure 3b. Labels for lines in (b) and (c) are same as those in (d). (e–h) Runs 13–15 with 50-km-thick crust. (e) Fraction of asthenosphere above 90-km depth. (f–h) Melting rates of different materials (in volume proportion per million years) above 100-km depth. The thick gray line is from Figure 3c. The horizontal plotting range is between 250 and 50 km to the left of the extensional center (or subsidence center of the surface; Figure 10). Note that melting in regions away from the locus of extension is largely depressed. Lith. M. = lithospheric mantle, Asthen. = asthenosphere, V_E = extension rate.

In regions close to the vertical weak zone, after 80 Ma the newly accreted materials form ~20–40% of the lithosphere (Figures 8a and 8e). Overall melting is dominated by mantle melting (Figures 8b–d and 8f–h). Crustal melting in the runs with 50-km-thick crust is clearly reduced (Figures 8f–8h).

In regions away from the initially preexisting vertical weak zone, former asthenosphere material only comprises ~20% of the regions shallower than 90 km (Figures 9a and 9e). Again, melting behavior is depressed compared to the conditions shown in Figure 6. Reduced melting is due to (1) that crust is thinned during extension (Figure 10), with associated enhanced cooling towards the Moho and (2) the intensive melting (>10%) during diapiric asthenospheric upwelling (Figure 10) consumes heat, so the intruded asthenosphere is cooler than temperatures achieved during large-scale convective erosion and reworking (Figures 7e and 10d).

4.3.1. Extension-Induced Lithospheric Replacement

Run 15 is taken as a type example for lithospheric modifications during extension.

As the lithosphere extends, asthenosphere and metasome material intrude upward utilizing a preexisting vertical weak zone (Figure 10b). This mushroom-shaped upwelling leads to a locally elevated temperature structure.

Upwelling mantle materials experience ~10–20% melting (Figure 10b), and they locally heat the lower crust to melting point at ~10 Ma (Figure 8h).

During subsequent extension, an increase is noted in the width of mantle upwelling and the lateral extent of melting (Figures 10c and 10d). After ~30 Ma, the shallow mantle gradually cools and convection ceases (Figure 10c). Subsequent deeper mantle convection reworks the still ductile lowermost lithosphere and modifies the shape of intruded mantle materials (Figure 10d). By ~80 Ma, the 1,300 °C potential temperature contours have recovered to >80-km depths.
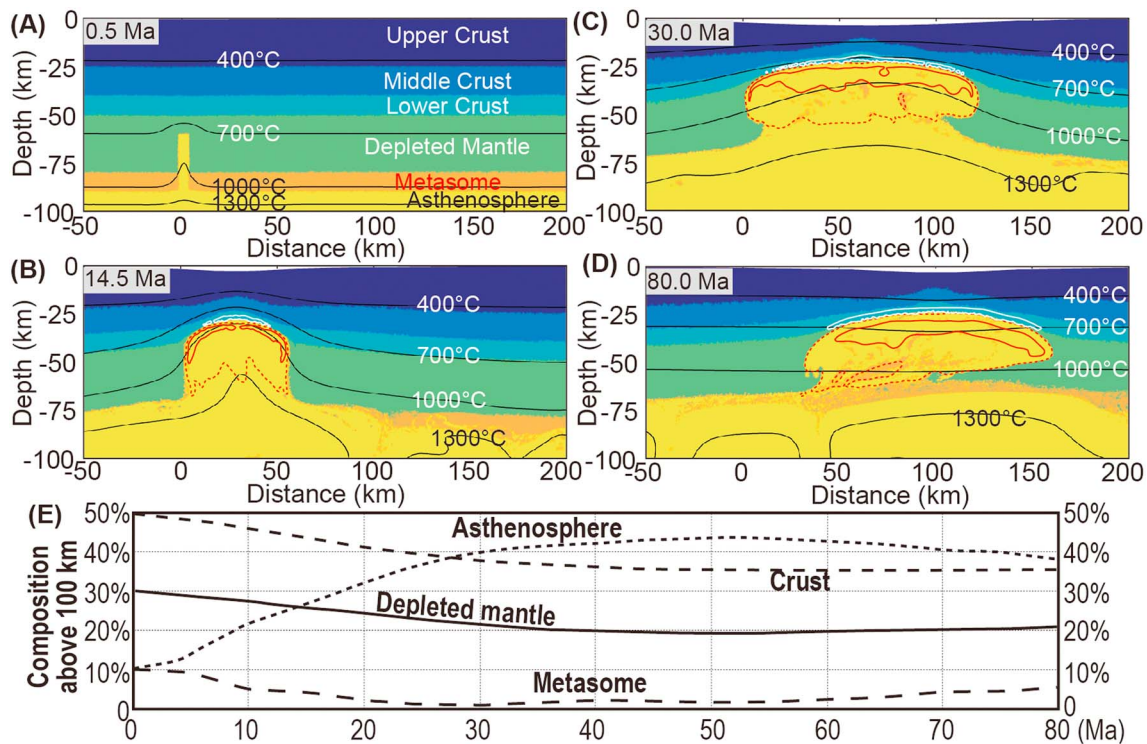
Figure 10. Lithospheric extension along a preexisting vertical weak zone (run 15). (a) Initial conditions of this run (see more details in Figure 5). (b) During lithospheric extension, asthenosphere and/or metasome material rises along the localized weak zone. These rising materials undergo decompression melting. (c) The volume of intruded materials grows, while further upwelling of mantle is resisted by the presence of overlying crust. The lower crust is stretched to locally disappear. (d) In the following evolution, the melting center migrates with the locus of extension. The shape of the upwelling structure evolves to a "mushroom"-like form similar to that observed in seismic records (compare to Figure 4). (e) Volume fractions of different materials above 100-km depth. Note that pockets of metasome material are entrained into later upwelling where they can experience further decompression melting (also see (c) and (d)). White lines mark the range of crustal melting. Red dashed lines are contours of mantle with depletion >10%. Red solid lines are contours of mantle with depletion >20%.

5. Discussion

5.1. Convective Erosion Driven by a Rayleigh–Taylor-Type Gravity Instability

Although most initial asthenospheric upwelling occurs close to the ends of depleted mantle layer in runs 1–8, the side boundary conditions themselves do not drive interface disturbances. The initial diapirs do not occur exactly along the left/right boundary (the insect panel in Figure 7b). Instead, they rise because the overlying material is stretched toward the sinking centers. This is a frequent characteristic of Rayleigh–Taylor-type gravity instabilities (cf. Conrad & Molnar, 1997). Previous studies illustrate that when a nonlinear viscosity is considered for the unstable layer, initial interface disturbances tend to focus at locations close to the edges of the layer (Canright & Morris, 1993; Harig et al., 2010; Houseman & Molnar, 1997). Our experiments reproduce this behavior. They show that (1) the initial downwelling and upwelling are separated due to the focusing of deformation during power law creep (cf. Canright & Morris, 1993) and (2) late-stage downwelling becomes more focused, while contemporaneous upwelling becomes more diffuse (Figure 7e). The convective erosion mode seen here resembles a gravitational instability in a power law creep material with a horizontal stress-free condition.

Unlike previous studies (Gorczyk et al., 2012; Harig et al., 2010; also see discussion in Part 1; Liu et al., 2018), the gravitational instability at the base of relic lithosphere does not lead to large-scale lithospheric downwelling blobs because the postdelamination cratonic mantle initially retains its high strength ($>10^{21}$ Pa s; Figure 7; cf. Djomani et al., 2001; Lenardic & Moresi, 1999; Sleep, 2003). Depleted mantle can only be separated from the base of the lithosphere in relatively small amounts (Figure 7). During this process >80% of depleted mantle remains relatively unaffected by convective erosion, with only

~10–20% mixing with asthenosphere (Figures 6a and 7f). Because the depleted mantle is assumed to be lack water (Sleep, 2003), melting would primarily occur in the water-enriched and less-refractory asthenosphere. This scenario is consistent with the observation that asthenospheric material is found to dominate the <80-Ma postdestruction basaltic magmas on the ENCC (Menzies et al., 2007; Hong et al., 2012; Xu, 2001; Xu et al., 2009).

5.2. The Role in Melting of a Preexisting Cratonic Metasome MLDL

The earliest approximately 190–155-Ma magmas on the ENCC primarily sourced a relatively cool, hydrous, mantle component with a composition consistent with the proposed metasomatic mantle layer (*metasome*) at ~80–100-km depths with a composition like that of exhumed water-rich MARID xenoliths (Dawson & Smith, 1977; Menzies & Zhang, 1993; Sweeney et al., 1993; Xu, 2001). In our preferred scenario (Figure 2), this geochemically implied metasomatic layer is proposed to be the critical weak layer that led to lower keel delamination (the topic of Part 1; Liu et al., 2018). Only after delamination, could relatively shallow melting on-cratonic magmatism occur. This proposition is supported by studies of seismic images and numerical modeling. See Part 1 for further details on the potential origin of a metasomatic MLD-linked metasome layer (Liu et al., 2018).

5.3. Onset and Distribution Patterns of On-Craton Magmas

On-craton magmatism occurred ~20 Ma earlier on the Northern ENCC than on its southern portions (Figure 3). Between approximately 150 and 100 Ma (Figure 11), three magmatic belts can be identified on the ENCC. These three belts appear to have been active for similar time scales, and are separated by a region free of magmatism (belt IV) in the central ENCC throughout approximately 150–100 Ma (Figure 11). Magmatism of belts I and III did not migrate across the region, while the magmatic center of belt I traveled eastward after approximately 130 Ma (Figure 11f).

In our preferred scenario, the onset of magmatism on the ENCC (Figure 3) is controlled by the sequence of the proceeding keel delamination. While geologically rapid, the delamination process itself can occur in jerks, with pulses of rapid delamination ending as a keel fragment breaks away (Figure 2a and details in Part 1; Liu et al., 2018). This implies that the earlier onset of magmatism on the northern regions (Figure 3) may indicate earlier keel delamination beneath them.

After the delamination of lower keel, overall heating of the remaining lithosphere may explain the approximately 190–155-Ma magmatism in the northern regions with thick crust and weak lithospheric extension (Figures 1b, 3a, and 6g–6i; Meng, 2003). In regions close to the Tan-Lu fault zone, delamination can have happened nearly coevally with the onset of lithospheric extension (approximately 160–150 Ma; He & Wang, 2004; Meng, 2003). Therefore, although these regions lacked thick crust, decompression melting during initial metasome/asthenosphere upwelling can have led to late first pulse magmatism at approximately 160–155 Ma (Figures 3b, 8b, and 8c).

Thereafter, mantle upwelling could lead to the second pulse of magmatism at approximately 135–115 Ma, in extension-free regions capped by thick crust (Figures 6g–6i) or in extensional regions that experienced focused thinning with associated asthenosphere intrusions into relic shallow cratonic lithosphere (Figures 8b and 8c). In the former scenario, magmatism would gradually expand from the margins toward the inner craton (Figure 7), while their distribution could still be concentrated in regions capped by thicker crust (i.e., the belt I in Figure 11). In the latter scenario, the area of magmatism grows as the region of focused intralithospheric upwelling expands, and the center of magmatism would move with the locus of lithospheric extension (Figure 10). This latter scenario may help to explain the distribution of the magmatism in regions close to the Tan-Lu fault zone (belt III in Figure 11). Later (approximately 160 Ma) delamination with nearly coeval extension of lithosphere capped by thick crust may help to explain the nearly continuous approximately 160–120-Ma magmatism along the southwestern ENCC (belt III in Figure 11; also see Figures 3c, 8g, and 8h).

As noted above, limited melting should occur beneath extension-free regions capped by ~40-km-thick crust (Figures 6c–6e). Even in scenarios with lithospheric extension, melting is mostly absent in regions away from the extensional center (Figure 9). In both situations, lower rates of mantle upwelling (Figures 6a, 9a, and 9e) and thin or thinned crust results in a cooler lithospheric geotherm and reduced melting. In this interpretation,
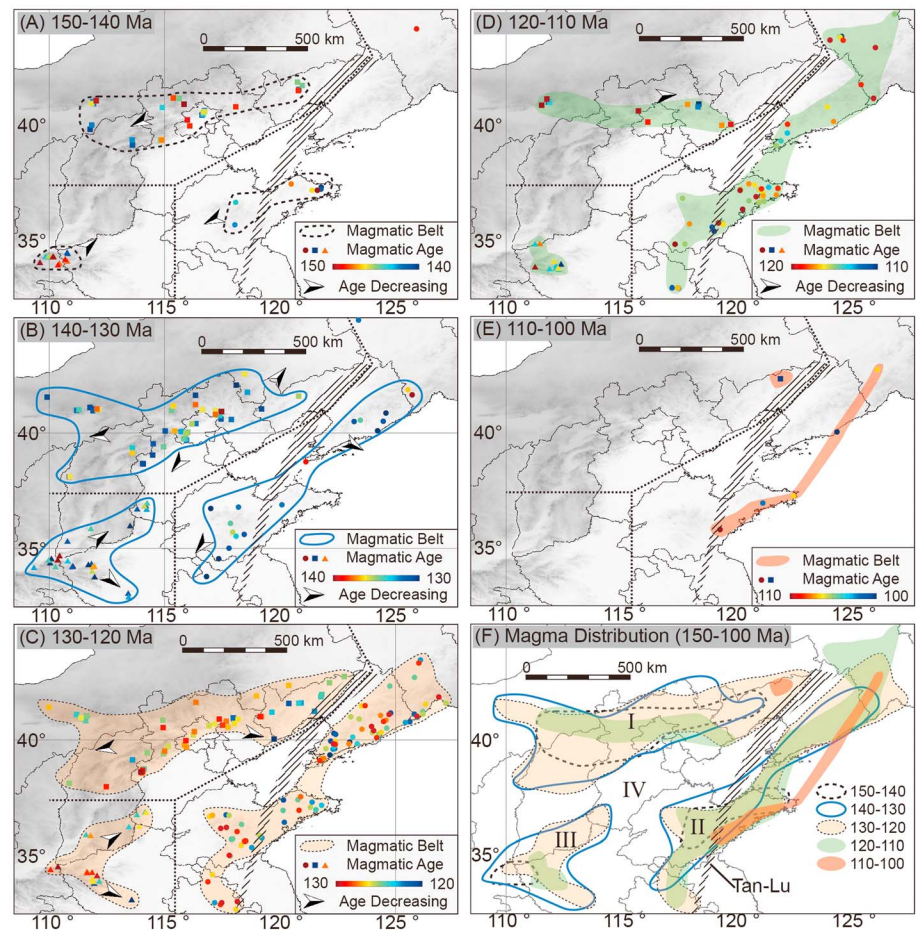
Figure 11. Distribution of magmas on the ENCC during approximately 150–100 Ma. (a–e) Distribution of magmas in five temporal snapshots. (f) A summary of data from (a)–(e). Three magmatic belts (I, II, and III) can be identified (crudely divided by black dots in (a)–(e)), their ranges expand after approximately 150 Ma, and peak between approximately 130 and 120 Ma. Belt IV is a magmatism free belt. Note that, after approximately 140 Ma, belts I and III expanded toward the inner ENCC; belt II expanded toward the northeast (in regions to the east of the northern tan-Lu), and toward the southwest (in regions to west of the southern tan-Lu). This is consistent with local crustal extension directions (Figure 1a); the data set of high-resolution magmatic dating (534 dates in total) is based upon the work of Zhang et al. (2014), with 64 recently published ages added to their published data (supplement II presents these data in tabular form). Tan-Lu: the Tancheng-Lujiang Fault zone.

the magma-free belt IV in Figure 11 formed because this region was initially capped by relatively thin crust (i.e., <40 km), and it lay far from extensional centers, i.e., the Tan-Lu fault zone.

5.4. Implications for the Origin of On-Cratonic Magmas

Initial on-cratonic magmas are primarily felsic in composition as by-products of lower crustal melting (Wu et al., 2005; Xu et al., 2009). According to the studies of zircon saturation temperature, the Jurassic (approximately 190–155 Ma) granitic magmas (~750 °C) in Liaodong are ~50–100 °C cooler than those with Cretaceous ages (approximately 135–115 Ma; Wu et al., 2007; Xu et al., 2009). This may indicate different triggers for crustal melting at these two stages, i.e., that fluids derived from subduction zones could have lowered the crustal solidus in Jurassic times (Wu et al., 2007).

As noted above, we propose that the source material for the minor mafic magmas observed in the Jurassic was the preexisting metasomatic (Menzies & Zhang, 1993; Xu, 2001) intracratonic MLDL. The numerical experiments indicate that melting of this enriched layer can explain the Jurassic magmas. We suggest that (1) the approximately 190–155-Ma magmatism was triggered by underplating of MLDL-derived melts and (2) the 135–115-Ma magmatism was created by shallower (~60–80 km deep)
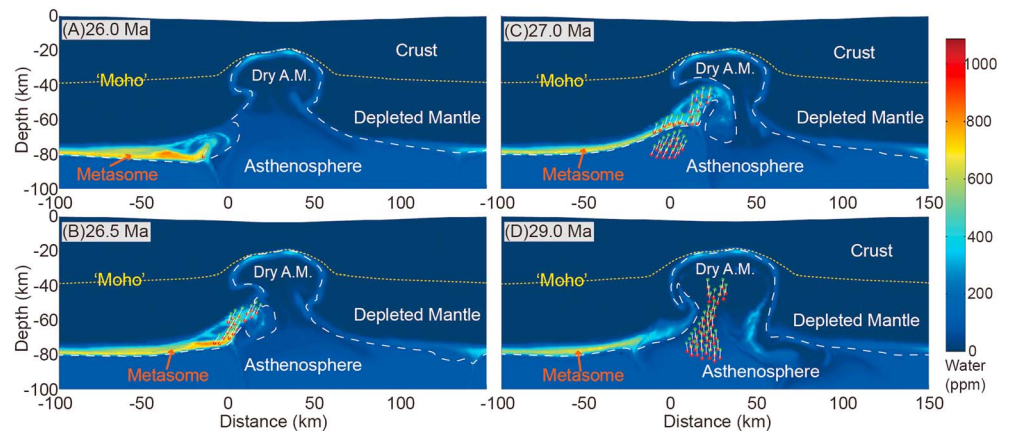
Figure 12. The metasome MLDL as a potential water-rich source for Cretaceous (approximately 120 Ma) basalts on the ENCC. Plots are made for the materials' water content (weight proportion in parts per million (ppm)) of run 10 (Table 2). (a) If cool enough, metasome material can remain locally stable at depths below 80 km deep. (b) Metasome material is entrained into the upwelling asthenosphere, experiences decompression melting, and releases water that can enhance melting of adjacent asthenosphere, in particular. (c) Upwelling asthenosphere also starts to melt. (d) Mixture of asthenosphere and metasome material becomes a primary magma source.

melting associated with upwelling during reworking of the asthenosphere, residual fragments of MLDL, and relic cratonic lithosphere.

5.4.1. 190–155-Ma Magmatism: Crustal Melting Triggered by Underplating

In the numerical experiments (Figures 6, 7, 8, 9, and 10), the first melting pulse is primarily due to deep (>80 km deep) melting of metasoma MLDL and/or asthenosphere, in apparent contradiction to observations that most of the approximately 190–155-Ma magmas are primarily felsic in composition, indicating an origin related to crustal melting (Wu et al., 2005; Xu et al., 2009). This inconsistency highlights a key oversimplification in our numerical model, namely, that it does not simulate the upward migration of melts that could lead to intruded mafic melts at the base of the crust. The accumulation of hot mafic melts at the base of the crust (cf. Bryan & Ferrari, 2013) could trigger minor melting of lower crust (with solidus of ~1050 °C, at ~50 km deep; Figure A1a), with the crustal melts being recorded as the Jurassic granites.

As in arc magmatism (Wu et al., 2007), the melts of deep low-degree melting of the metasoma + asthenosphere can also be rich in water that lowers the solidus of crust. Therefore, the underplating origin may help to explain the low saturation temperature of zircons in the Jurassic granites (Wu et al., 2007). Because the metasome MLDL contains higher proportions of volatiles than asthenosphere, its melting products may also more easily overcome the crustal buoyancy filter and be expressed as the observed minor amounts of approximately 190–155-Ma mafic magmas (Xu, 2001; Xu et al., 2009).

5.4.2. 135–115-Ma Magmatism: Melting Related to Upwelling

The numerical experiments imply that the 135–115-Ma magmatism on the ENCC was induced by even shallower upwelling of asthenosphere and residual metasome (Figures 6, 7, 8, 9, and 10).

Due to the low partition coefficients of volatiles (cf. Aubaud et al., 2004), most of the volatile content in the original metasoma MLDL and asthenosphere would have been lost during the approximately 190–155-Ma low-degree melting stage. Thus, products of shallower melting during approximately 135–115 Ma should not release as much water to lower the solidus of overlying crust. This is consistent with the Cretaceous granites having a higher zircon temperature than that of the Jurassic granites (Wu et al., 2007).

As asthenosphere rises to <60 km that allowing higher degrees of melting (Figures 7e and 10c), its contribution in magmatic source may increase (Figures 6, 8 and 9), consistent with observations on mafic magmas younger than approximately 160 Ma (Xu, 2001; Xu et al., 2009). Note that, during this second pulse of melting, the asthenosphere is still not the only mantle material that melts (Figures 6, 8, and 9). Metasome material also melts when entrained into later upwellings (Figures 10e and 12). This may have contributed to the water-rich mantle source of the ~120-Ma basaltic lavas close to the Tan-Lu fault zone (Xia et al., 2013).
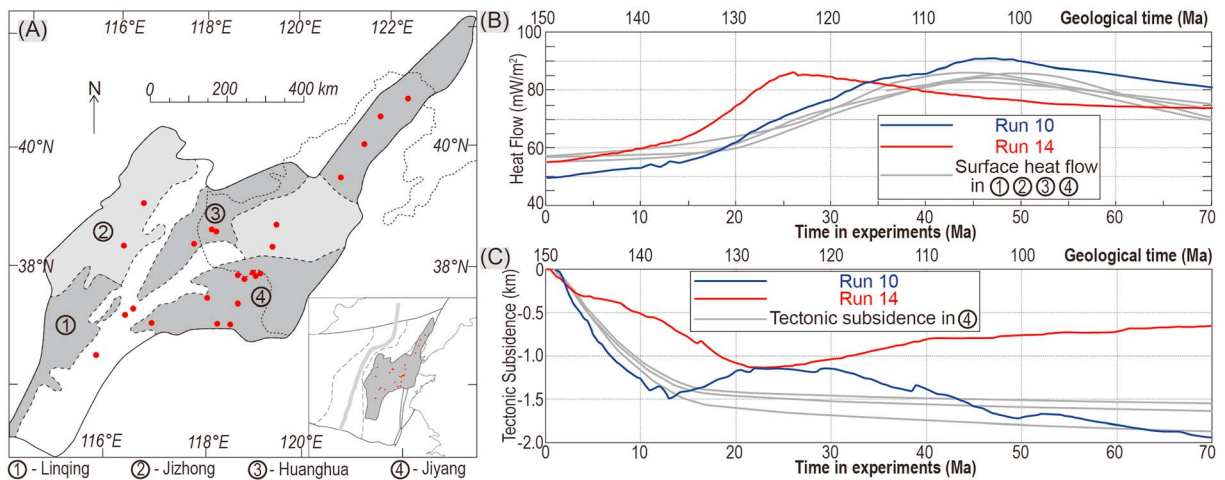
Figure 13. Comparison between numerical experimental results and the geologic/geophysical record preserved in rift basins. (a) Locations for wells (red dots) that provide data for reconstructions of surface heat flow. ①–④ are names for syn-destruction rift basins. (b) Comparison between numerical experimental results and reconstructions of surface heat flow (gray lines; Qiu et al., 2016). (c) Comparison between numerical experimental results and reconstructions of tectonic subsidence (gray lines; He & Wang, 2004).

In these models, a second pulse of crustal melting only occurs in the experiments with 50-km-thick crust and no lithospheric extension (Figures 6, 8, and 9). The lower initial Moho temperature in experiments with thinner initial crust does not favor crustal melting.

In scenarios without extension, the slow ascent of asthenosphere during convective erosion gradually heats up the surrounding lithosphere. The asthenosphere itself cools down, experiences low-degree (~5%) melting, and loses most of its heat through conduction (Figure 7). When the Moho temperature is hot enough (here, in the scenario with 50-km-thick crust), lower crustal melting can occur. The melting material at this stage is composed of lower crust, ancient relic mantle, and asthenosphere.

In scenarios with extension, more rapidly rising asthenosphere loses significant heat by large-degree (>10%) decompression melting. In addition, the thinner crust induced by stretching cools faster, leading to a cooler Moho. Therefore, direct crustal melting does not occur. As noted above, the absence of crustal melting at times of potential underplating of mafic magmas at the Moho is due to limitations in our current numerical method.

5.5. How Was the Inhomogeneous Lithospheric Mantle Created?

In previous studies, syn-cratonic destruction lithospheric extension and the existing of localized translithospheric weaknesses (e.g., the Tan-Lu fault zone) are suggested to be important in creating the inhomogeneous mantle beneath the modern ENCC (Hao et al., 2013; Menzies et al., 2007; Xu et al., 2002; Yuan, 1996). Our results generally support this suggestion.

During lithospheric extension, the translithospheric weak zone can allow ascent of asthenosphere + metasome material (Figure 10). Rising material often assumes a crude "mushroom-like" form like those revealed in seismic studies (Figure 4). The upwelling mantle material is predicted to release ~10–20% (volume percent) mafic melts, which may lead to melt underplating and re-thickening of the mafic lower crustal layer (Thybo & Artemieva, 2013; Thybo & Nielsen, 2009). Compared with intermediate-felsic rocks, underplating mafic melts have a higher P wave velocity (Christensen & Mooney, 1995; Gao et al., 1998). This appears to be consistent with seismic studies (Hao et al., 2013; Xu et al., 2002), as the mushroom anomalies are typically underlain by high-velocity anomalies within the overlying crust (Figures 4b and 4c). The results are also consistent with the observations that the lower crustal thickness in extensional regions appears to be noticeably thicker (~10 km) than the thicknesses beneath extension-free inner cratonic areas (<5 km; Deng et al., 2013; Gao et al., 1998; Xia et al., 2017).

The evolution of surface heat flow and tectonic subsidence in the numerical results is also crudely consistent with the geologic record above mushroom-shaped velocity anomalies (Figure 13). Scenarios with an initial 40-km-thick crust appear to better match the crude observations.

Convective erosion in regions without strong lithospheric extension can also help to explain the petrological and geochemical heterogeneity of the ENCC mantle (Figures 7e and 7f). According to the modeling results, the local replacement rate is predicated to be ~10–20% (Figures 6a, 6f, and 7f). Because newly accreted material has experienced ~5–10% partial melting, its solidus can remain lower than that of dry, refractory relic cratonic mantle that once experienced >30% melting (Lee et al., 2011). As a consequence, postdestruction magmas can preferentially sample newly emplaced mantle (Hong et al., 2012; Xu, 2001; Xu et al., 2009).

6. Conclusions

In this paper, we explored the second postkeel-delamination stage of a two-stage craton destruction model, examining its implications for the recent evolution of the ENCC. In the proposed model, (1) the lower keel (below ~80–100 km) rapidly delaminates along an intracratonic weak layer within 20–10 Ma and (2) after keel delamination along an 80–100-km-deep MLDL, the relic lithosphere and MLDL material come into contact with hotter asthenosphere. The MLDL material heats up and undergoes partial melting, while the relic reworked lithosphere and intruding asthenosphere and MLDL material become more heterogeneous during a postdelamination evolution (80–60 Ma) that is dominated by lithospheric reworking involving convective-erosion and/or lithospheric-extension. Our conclusions are the following:

1. The 190–155-Ma "cold" felsic magmas on the ENCC are suggested to be produced by the crustal underplating of water-rich melts that derived from the melting of a possible mixture of enriched metasome layer ± asthenosphere at >80-km depths. Subsequent 135–115-Ma magmatism is due to shallower mantle upwelling that develops during progressive convective erosion and lithospheric extension.
2. The distribution of magmas is strongly shaped by the initial distribution of thicker (i.e., 50 km) crust and of translithospheric weak zones. In regions capped by ~50-km-thick crust, for example, the northern margin of the ENCC, two pulses of magmatism occur during convective erosion of the relic lithosphere. In regions close to translithospheric weaknesses (e.g., the Tan-Lu fault zone), multiple pulses of magmatism happen during pulses(?) of lithospheric extension. In regions capped by thin/thinned crust (<40 km thick) that does not undergo extension, syn-destruction magmatism is rare.
3. Lithosphere-scale faults or localized weak zones help to initiate sublithospheric mantle upwelling at depth. Their presence can lead to the extension-linked creation of seismic mushroom anomalies found close to the Tan-Lu fault zone.
4. The petrological and geochemical heterogeneity of the modern ENCC mantle is due to both lithospheric extension and convective erosion, which have led to ~10–30% ancient cratonic mantle being replaced by asthenosphere + residues to melting of metasome MLDL.

Appendix A

This appendix describes the additional algorithms used here for numerical experiments that were not presented in the appendix of Part 1 (Liu et al., 2018).

A1. Density

Material density depends on temperature, pressure, depletion, and water dependency (Djomani et al., 2001; Richard & Bercovici, 2009; Schutt & Lesher, 2006; Turcotte & Schubert, 2014):

$$\rho = \left(\left(1 - f + f\frac{\rho_{0molten}}{\rho_{0solid}} - \beta H \right) \exp\left[-\int_{T_0}^{T_F} \alpha(P = P_0, T)dT + \int_{P_0}^{P_F} \frac{dP}{k} \right] \right) \quad \text{(A1)}$$

where the thermal expansion coefficient $\alpha = a_1 + a_2 T + a_3 T^{-2}$, ρ_{0solid}, and $\rho_{0molten}$ (2.9 g/cm^3 for mantle and 2.7/cm^3 for crust) are solid density and melt density at room temperature ($T_0 = 20$ °C) and pressure ($P_0 = 0.1$ MPa), k is the bulk modulus, T_F and P_F are the temperature and pressure during calculation, f is the depletion, H is the water content in terms of weight fraction, and β is a coefficient expressing the linear dependency of the density on water content (0.025 wt.% H_2O^{-1}; cf. Richard & Bercovici, 2009).
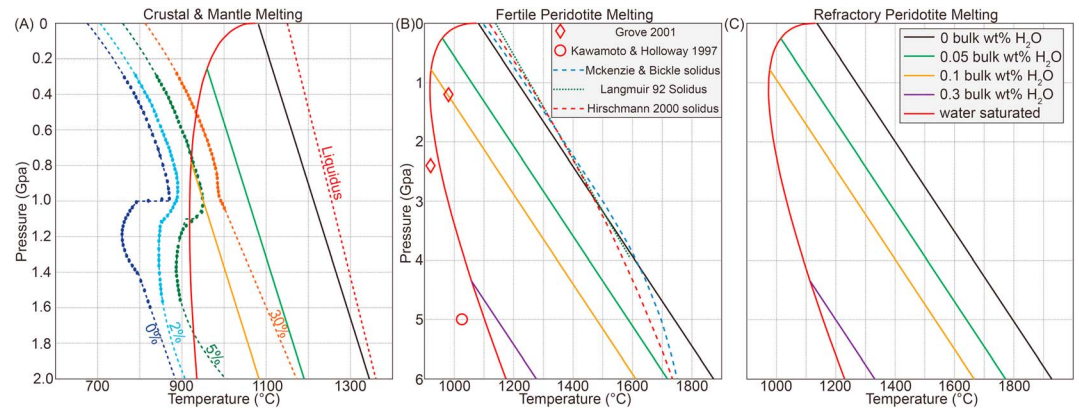
Figure A1. (a) Crustal solidus. Dots in (a) are the measured solidus for amphibolite with varying degrees of depletion (López & Castro, 2001). Two percent means that amphibolite has experienced 2% melt extraction. Dashed lines are the numerically fitted solidus used in modeling. Solid lines are mantle solidus from (b). (b) Asthenospheric/metasome material (fertile mantle) solidus. (c) Lithospheric mantle (depleted mantle) solidus. The effect of dissolved water on the solidus is linear and bounded by the saturation of water in the melt (Katz et al., 2003). The "0.05 bulk wt.%" refers to the water content used for calculating the solidus.

A2. Effective Viscosity

The effective viscosity μ_{eff} is calculated in the form of Moresi et al. (2003), considering contributions from diffusion and dislocation creep, elasticity, and plasticity:

$$\mu_{\mathrm{eff}} = S \cdot \left[\eta_{\mathrm{dis}}^{-1} + \eta_{\mathrm{dif}}^{-1} + (\Delta t G)^{-1} + \Gamma_{\mathrm{II}}/\Gamma_0 \right]^{-1} \tag{A2}$$

where η_{dis} is the viscosity in dislocation creep, η_{dif} is the viscosity in diffusion creep, Δt is the time step during calculation, G is the shear modulus, Γ_0 is the yielding plastic potential (equation (A3)), Γ_{II} is the square root of the second invariant of deviatoric stress, and S is the strain-weakening coefficient (see the Appendix of Part 1 (Liu et al., 2018)).

$$\Gamma_0 = P \sin(\varphi) + c \cos(\varphi) \tag{A3}$$

where P is the pressure, c is the yielding cohesion, and φ is the friction angle.

Γ_0 in equation (A2) is 0 when $\Gamma_{\mathrm{II}} < \Gamma_0$. If yielding occurs $\Gamma_{\mathrm{II}} \geq \Gamma_0$, the effective viscosity on the yielding point is calculated by

$$\mu_{\mathrm{eff}} = \Gamma_0/\Gamma_{\mathrm{II}} \tag{A4}$$

A3. Mantle and Crustal Melting

We use the method in Part 1 (Liu et al., 2018) to determine melting regions. Parameters of crustal melting, for example, the solidus at room temperature and pressure T_0^m, the solidus's dependence on degree of melting $(\partial T^m/\partial f)_P$, and the solidus's dependence on pressure $(\partial T^m/\partial P)_f$, are crudely estimated by numerically fitting experimental results for melting of amphibolite (Figure A1a; López & Castro, 2001).

A4. Dehydration Process

Potential dehydration of water-rich materials (e.g., asthenosphere and metasome) is only crudely considered following the approach of Gerya and Meilick (2011). A 1 wt% water content is set to be the maximum solubility for each material. When melting happens, new water tracers are added to track the evolution of water content. These tracers are advected every time step in a Lagrangian form. Their horizontal velocities are interpolated from the element they belong to, and their vertical velocities are set to be 10 cm/year (Figure 12). Water in a tracer will be released to the material it encounters if this material's water content is lower than 1 wt%. Once all water is removed from a tracer, it is deleted.

Journal of Geophysical Research: Solid Earth

References

Andrés-Martínez, M., Morgan, J. P., Pérez-Gussinyé, M., & Rüpke, L. (2015). A new free-surface stabilization algorithm for geodynamical modelling: Theory and numerical tests. *Physics of the Earth and Planetary Interiors*, 246, 41–51. https://doi.org/10.1016/j.pepi.2015.07.003

Aubaud, C., Hauri, E. H., & Hirschmann, M. M. (2004). Hydrogen partition coefficients between nominally anhydrous minerals and basaltic melts. *Geophysical Research Letters*, 31, L20611. https://doi.org/10.1029/2004GL021341

Bird, P. (1979). Continental delamination and the Colorado Plateau. *Journal of Geophysical Research*, 84(Nb13), 7561–7571. https://doi.org/10.1029/JB084iB13p07561

Brune, S., Heine, C., Perez-Gussinye, M., & Sobolev, S. V. (2014). Rift migration explains continental margin asymmetry and crustal hyper-extension. *Nature Communications*, 5(1), 4014. https://doi.org/10.1038/ncomms5014

Bryan, S. E., & Ferrari, L. (2013). Large igneous provinces and silicic large igneous provinces: Progress in our understanding over the last 25 years. *Bulletin of the Geological Society of America*, 125(7–8), 1053–1078. https://doi.org/10.1130/B30820.1

Canright, D., & Morris, S. (1993). Buoyant instability of a viscous film over a passive fluid. *Journal of Fluid Mechanics*, 255(1), 349–372. https://doi.org/10.1017/S0022112093002514

Chen, L., Jiang, M. M., Yang, J. H., Wei, Z. G., Liu, C. Z., & Ling, Y. (2014). Presence of an intralithospheric discontinuity in the central and western North China craton: Implications for destruction of the craton. *Geology*, 42(3), 223–226. https://doi.org/10.1130/G35010.1

Christensen, N. I., & Mooney, W. D. (1995). Seismic velocity structure and composition of the continental crust: A global view. *Journal of Geophysical Research*, 100(B6), 9761–9788. https://doi.org/10.1029/95JB00259

Conrad, C. P., & Molnar, P. (1997). The growth of Rayleigh-Taylor-type instabilities in the lithosphere for various rheological and density structures. *Geophysical Journal International*, 129(1), 95–112. https://doi.org/10.1111/j.1365-246X.1997.tb00939.x

Dawson, J. B., & Smith, J. V. (1977). The MARID (mica-amphibole-rutile-ilmenite-diopside) suite of xenoliths in kimberlite. *Geochimica et Cosmochimica Acta*, 41(2), 309–310. https://doi.org/10.1016/0016-7037(77)90239-3

Deng, Y. F., Fan, W. M., Zhang, Z. J., & Badal, J. (2013). Geophysical evidence on segmentation of the Tancheng-Lujiang fault and its implications on the lithosphere evolution in East China. *Journal of Asian Earth Sciences*, 78, 263–276. https://doi.org/10.1016/j.jseaes.2012.11.006

Djomani, Y. H. P., O'Reilly, S. Y., Griffin, W. L., & Morgan, P. (2001). The density structure of subcontinental lithosphere through time. *Earth and Planetary Science Letters*, 184(3–4), 605–621. https://doi.org/10.1016/S0012-821X(00)00362-9

Gao, S., Luo, T. C., Zhang, B. R., Zhang, H. F., Han, Y. W., Zhao, Z. D., & Hu, Y. K. (1998). Chemical composition of the continental crust as revealed by studies in East China. *Geochimica et Cosmochimica Acta*, 62(11), 1959–1975. https://doi.org/10.1016/S0016-7037(98)00121-5

Gao, S., Rudnick, R. L., Yuan, H. L., Liu, X. M., Liu, Y. S., Xu, W. L., et al. (2004). Recycling lower continental crust in the North China craton. *Nature*, 432(7019), 892–897. https://doi.org/10.1038/nature03162

Gerya, T. V., Connolly, J. A. D., Yuen, D. A., Gorczyk, W., & Capel, A. M. (2006). Seismic implications of mantle wedge plumes. *Physics of the Earth and Planetary Interiors*, 156(1–2), 59–74. https://doi.org/10.1016/j.pepi.2006.02.005

Gerya, T. V., & Meilick, F. I. (2011). Geodynamic regimes of subduction under an active margin: Effects of rheological weakening by fluids and melts. *Journal of Metamorphic Geology*, 29(1), 7–31. https://doi.org/10.1111/j.1525-1314.2010.00904.x

Gerya, T. V., & Yuen, D. A. (2003). Rayleigh–Taylor instabilities from hydration and melting propel 'cold plumes' at subduction zones. *Earth and Planetary Science Letters*, 212(1-2), 47–62. https://doi.org/10.1016/S0012-821X(03)00265-6

Gleason, G. C., & Tullis, J. (1995). A flow law for dislocation creep of quartz aggregates determined with the molten salt cell. *Tectonophysics*, 247(1-4), 1–23. https://doi.org/10.1016/0040-1951(95)00011-B

Gorczyk, W., Hobbs, B., & Gerya, T. (2012). Initiation of Rayleigh-Taylor instabilities in intra-cratonic settings. *Tectonophysics*, 514-517, 146–155. https://doi.org/10.1016/j.tecto.2011.10.016

Griffin, W. L., Andi, Z., O'Reilly, S. Y., & Ryan, C. G. (1998). Phanerozoic evolution of the lithosphere beneath the Sino-Korean craton. *Mantle Dynamics and Plate Interactions in East Asia*, 27, 107–126. https://doi.org/10.1029/GD027p0107

Griffin, W. L., O'Reilly, S. Y., Afonso, J. C., & Begg, G. C. (2009). The composition and evolution of lithospheric mantle: A re-evaluation and its tectonic implications. *Journal of Petrology*, 50(7), 1185–1204. https://doi.org/10.1093/petrology/egn033

Hao, T. Y., You, Q. Y., Liu, L. H., Lv, C. C., Xu, Y., Li, Z. W., et al. (2013). Joint land-sea seismic survey and research on the deep structures of the Bohai Sea areas. *Acta Oceanologica Sinica*, 32(12), 13–24. https://doi.org/10.1007/s13131-013-0383-4

Harig, C., Molnar, P., & Houseman, G. A. (2010). Lithospheric thinning and localization of deformation during Rayleigh-Taylor instability with nonlinear rheology and implications for intracontinental magmatism. *Journal of Geophysical Research*, 115, B02205. https://doi.org/10.1029/2009JB006422

Hasenclever, J. (2010). *Modeling mantle flow and melting processes at Mid-Ocean ridges and subduction zones—Development and application of numerical models* (Doctoral dissertation, Hamburg University). Retrieved from http://ediss.sub.uni-hamburg.de/volltexte/2010/4873/

Hasenclever, J., Morgan, J. P., Hort, M., & Rupke, L. H. (2011). 2D and 3D numerical models on compositionally buoyant diapirs in the mantle wedge. *Earth and Planetary Science Letters*, 311(1–2), 53–68. https://doi.org/10.1016/j.epsl.2011.08.043

He, L., & Wang, J. (2004). Tectono-thermal modelling of sedimentary basins with episodic extension and inversion, a case history of the Jiyang Basin, North China. *Basin Research*, 16(4), 587–599. https://doi.org/10.1111/j.1365-2117.2004.00245.x

He, L. J. (2014). Numerical modeling of convective erosion and peridotite-melt interaction in big mantle wedge: Implications for the destruction of the North China craton. *Journal of Geophysical Research: Solid Earth*, 119, 3662–3677. https://doi.org/10.1002/2013JB010657

Hirschmann, M. M., Aubaud, C., & Withers, A. C. (2005). Storage capacity of H_2O in nominally anhydrous minerals in the upper mantle. *Earth and Planetary Science Letters*, 236(1-2), 167–181. https://doi.org/10.1016/j.epsl.2005.04.022

Hirth, G., & Kohlstedt, D. (2004). Rheology of the upper mantle and the mantle wedge: A view from the experimentalists. In J. Eiler (Ed.), *Inside the Subduction Factory. Geophysical Monograph Series* (Vol. 138, pp. 83–105). Washington, DC: American Geophysical Union. https://doi.org/10.1029/138GM06

Hong, L.-B., Xu, Y.-G., Ren, Z.-Y., Kuang, Y.-S., Zhang, Y.-L., Li, J., et al. (2012). Petrology, geochemistry and Re–Os isotopes of peridotite xenoliths from Yantai, Shandong Province: Evidence for Phanerozoic lithospheric mantle beneath eastern North China Craton. *Lithos*, 155, 256–271.

Houseman, G. A., & Molnar, P. (1997). Gravitational (Rayleigh-Taylor) instability of a layer with non-linear viscosity and convective thinning of continental lithosphere. *Geophysical Journal International*, 128(1), 125–150. https://doi.org/10.1111/j.1365-246X.1997.tb04075.x

Jiang, G., Tang, X., Rao, S., Gao, P., Zhang, L., Zhao, P., & Hu, S. (2016). High-quality heat flow determination from the crystalline basement of the south-east margin of North China craton. *Journal of Asian Earth Sciences*, 118, 1–10. https://doi.org/10.1016/j.jseaes.2016.01.009

Karato, S. I., Olugboji, T., & Park, J. (2015). Mechanisms and geologic significance of the mid-lithosphere discontinuity in the continents. *Nature Geoscience*, 8(7), 509–514. https://doi.org/10.1038/NGEO2462

Katz, R. F., Spiegelman, M., & Langmuir, C. H. (2003). A new parameterization of hydrous mantle melting. *Geochemistry, Geophysics, Geosystems*, *4*(9), 1073. https://doi.org/10.1029/2002GC000433

Kay, R. W., & Kay, S. M. (1993). Delamination and delamination magmatism. *Tectonophysics*, *219*(1–3), 177–189. https://doi.org/10.1016/0040-1951(93)90295-U

Kinck, J. J., Husebye, E. S., & Larsson, F. R. (1993). The Moho depth distribution in Fennoscandia and the regional tectonic evolution from Archean to Permian times. *Precambrian Research*, *64*(1–4), 23–51. https://doi.org/10.1016/0301-9268(93)90067-C

Korenaga, J., & Karato, S. I. (2008). A new analysis of experimental data on olivine rheology. *Journal of Geophysical Research*, *113*, B02403. https://doi.org/10.1029/2007JB005100

Lee, C.-T. A., Luffi, P., & Chin, E. J. (2011). Building and destroying continental mantle. *Annual Review of Earth and Planetary Sciences*, *39*(1), 59–90. https://doi.org/10.1146/annurev-earth-040610-133505

Lenardic, A., & Moresi, L.- N. (1999). Some thoughts on the stability of cratonic lithosphere: Effects of buoyancy and viscosity. *Journal of Geophysical Research*, *104*(B6), 12,747–12,758. https://doi.org/10.1029/1999JB900035

Liao, J., & Gerya, T. (2014). Influence of lithospheric mantle stratification on craton extension: Insight from two-dimensional thermo-mechanical modeling. *Tectonophysics*, *631*, 50–64. https://doi.org/10.1016/j.tecto.2014.01.020

Liao, J., Wang, Q., Gerya, T., & Ballmer, M. D. (2017). Modeling craton destruction by hydration-induced weakening of the upper mantle. *Journal of Geophysical Research: Solid Earth*, *122*, 7449–7466. https://doi.org/10.1002/2017JB014157

Lin, G., Zhang, Y., Guo, F., Wang, Y. J., & Fan, W. M. (2005). Numerical modelling of lithosphere evolution in the North China block: Thermal versus tectonic thinning. *Journal of Geodynamics*, *40*(1), 92–103. https://doi.org/10.1016/j.jog.2005.07.011

Liu, L., Morgan, J., Xu, Y., & Menzies, M. (2016). Numerical modelling of the destruction of the Eastern North China Craton, paper presented at AGU Fall Meeting Abstracts, Abstract T11B-2624.

Liu, L., Morgan, J. P., Xu, Y., & Menzies, M. (2018). Craton destruction part 1: Cratonic keel delamination along a weak mid-lithospheric discontinuity layer. *Journal of Geophysical Research: Solid Earth*, *123*, 10,040–10,068. https://doi.org/10.1029/2017JB015372

López, S., & Castro, A. (2001). Determination of the fluid–absent solidus and supersolidus phase relationships of MORB-derived amphibolites in the range 4–14 kbar. *American Mineralogist*, *86*(11–12), 1396–1403. https://doi.org/10.2138/am-2001-11-1208

Meng, Q.-R. (2003). What drove late Mesozoic extension of the northern China–Mongolia tract? *Tectonophysics*, *369*(3-4), 155–174. https://doi.org/10.1016/S0040-1951(03)00195-1

Menzies, M., Xu, Y. G., Zhang, H. F., & Fan, W. M. (2007). Integration of geology, geophysics and geochemistry: A key to understanding the North China craton. *Lithos*, *96*(1–2), 1–21. https://doi.org/10.1016/j.lithos.2006.09.008

Menzies, W. F., & Zhang, M. (1993). Palaeozoic and Cenozoic lithoprobes and the loss of >120 km of Archaean lithosphere, Sino-Korean craton, China. *Geological Society, London, Special Publications*, *76*(1), 71–81. https://doi.org/10.1144/GSL.SP

Moresi, L., Dufour, F., & Muhlhaus, H. B. (2003). A Lagrangian integration point finite element method for large deformation modeling of viscoelastic geomaterials. *Journal of Computational Physics*, *184*(2), 476–497. https://doi.org/10.1016/S0021-9991(02)00031-1

Morgan, J. P. (2001). Thermodynamics of pressure release melting of a veined plum pudding mantle. *Geochemistry, Geophysics, Geosystems*, *2*(4). https://doi.org/10.1029/2000GC000049

Niu, Y. (2005). Generation and evolution of basaltic magmas: Some basic concepts and a new view on the origin of Mesozoic–Cenozoic basaltic volcanism in eastern China. *Geological Journal of China Universities*, *11*(1), 9–46.

Pollitz, F. F., Wicks, C., & Thatcher, W. (2001). Mantle flow beneath a continental strike-slip fault: Postseismic deformation after the 1999 Hector mine earthquake. *Science*, *293*(5536), 1814–1818. https://doi.org/10.1126/science.1061361

Qiu, N. S., Zuo, Y. H., Xu, W., Li, W. Z., Chang, J., & Zhu, C. Q. (2016). Meso-Cenozoic lithosphere thinning in the eastern North China craton: Evidence from thermal history of the Bohai Bay basin, North China. *Journal of Geology*, *124*(2), 195–219. https://doi.org/10.1086/684830

Rapp, R. P., & Watson, E. B. (1995). Dehydration melting of metabasalt at 8–32 kbar: Implications for continental growth and crust-mantle recycling. *Journal of Petrology*, *36*(4), 891–931. https://doi.org/10.1093/petrology/36.4.891

Richard, G. C., & Bercovici, D. (2009). Water-induced convection in the Earth's mantle transition zone. *Journal of Geophysical Research*, *114*, B01205. https://doi.org/10.1029/2008JB005734

Rutter, E., & Brodie, K. (2004). Experimental grain size-sensitive flow of hot-pressed Brazilian quartz aggregates. *Journal of Structural Geology*, *26*(11), 2011–2023. https://doi.org/10.1016/j.jsg.2004.04.006

Rybacki, E., & Dresen, G. (2004). Deformation mechanism maps for feldspar rocks. *Tectonophysics*, *382*(3-4), 173–187. https://doi.org/10.1016/j.tecto.2004.01.006

Schutt, D. L., & Lesher, C. E. (2006). Effects of melt depletion on the density and seismic velocity of garnet and spinel lherzolite. *Journal of Geophysical Research*, *111*, B05401. https://doi.org/10.1029/2003JB002950

Selway, K., Ford, H., & Kelemen, P. (2015). The seismic mid-lithosphere discontinuity. *Earth and Planetary Science Letters*, *414*, 45–57. https://doi.org/10.1016/j.epsl.2014.12.029

Sleep, N. H. (2003). Survival of Archean cratonal lithosphere. *Journal of Geophysical Research*, *108*(B6), 2302. https://doi.org/10.1029/2001JB000169

Sweeney, R., Thompson, A., & Ulmer, P. (1993). Phase relations of a natural MARID composition and implications for MARID genesis, lithospheric melting and mantle metasomatism. *Contributions to Mineralogy and Petrology*, *115*(2), 225–241. https://doi.org/10.1007/BF00321222

Thybo, H., & Artemieva, I. M. (2013). Moho and magmatic underplating in continental lithosphere. *Tectonophysics*, *609*(1), 605–619. https://doi.org/10.1016/j.tecto.2013.05.032

Thybo, H., & Nielsen, C. A. (2009). Magma-compensated crustal thinning in continental rift zones. *Nature*, *457*(7231), 873–876. https://doi.org/10.1038/nature07688

Turcotte, D. L., & Schubert, G. (2014). *Geodynamics* (p. 623). Cambridge: Cambridge University Press.

Wang, Z. S., Kusky, T. M., & Capitanio, F. A. (2016). Lithosphere thinning induced by slab penetration into a hydrous mantle transition zone. *Geophysical Research Letters*, *43*, 11,567–11,577. https://doi.org/10.1002/2016GL071186

Wenker, S., & Beaumont, C. (2017). Can metasomatic weakening result in the rifting of cratons? *Tectonophysics*, 0040-1951. https://doi.org/10.1016/j.tecto.2017.06.013

Wilks, K. R., & Carter, N. L. (1990). Rheology of some continental lower crustal rocks. *Tectonophysics*, *182*(1-2), 57–77. https://doi.org/10.1016/0040-1951(90)90342-6

Wu, F. Y., Li, X. H., Yang, J. H., & Zheng, Y. F. (2007). Discussions on the petrogenesis of granites (*in Chinese*). *Acta Petrologica Sinica*. https://doi.org/10.3969/j.issn.1000-0569.2007.06.001

Wu, F. Y., Yang, J. H., Wilde, S. A., & Zhang, X. O. (2005). Geochronology, petrogenesis and tectonic implications of Jurassic granites in the Liaodong peninsula, NE China. *Chemical Geology*, *221*(1–2), 127–156. https://doi.org/10.1016/j.chemgeo.2005.04.010

Xia, B., Thybo, H., & Artemieva, I. M. (2017). Seismic crustal structure of the North China craton and surrounding area: Synthesis and analysis. *Journal of Geophysical Research: Solid Earth*, *122*, 5181–5207. https://doi.org/10.1002/2016JB013848

Xia, Q. K., Liu, J., Liu, S. C., Kovacs, I., Feng, M., & Dang, L. (2013). High water content in Mesozoic primitive basalts of the North China craton and implications on the destruction of cratonic mantle lithosphere. *Earth and Planetary Science Letters*, *361*, 85–97. https://doi.org/10.1016/j.epsl.2012.11.024

Xu, P. F., Liu, F. T., Ye, K., Wang, Q. C., Cong, B. L., & Chen, H. (2002). Flake tectonics in the Sulu orogen in eastern China as revealed by seismic tomography. *Geophysical Research Letters*, *29*(10), 1385. https://doi.org/10.1029/2001GL014185

Xu, Y. G. (2001). Thermo-tectonic destruction of the archaean lithospheric keel beneath the Sino-Korean craton in China: Evidence, timing and mechanism. *Physics and Chemistry of the Earth, Part A*, *26*(9–10), 747–757. https://doi.org/10.1016/S1464-1895(01)00124-7

Xu, Y. G., Li, H. Y., Pang, C. J., & He, B. (2009). On the timing and duration of the destruction of the North China craton. *Chinese Science Bulletin*, *54*(19), 3379–3396. https://doi.org/10.1007/s11434-009-0346-5

Yang, J., Zhao, L., Kaus, B. J., Lu, G., Wang, K., & Zhu, R. (2017). Slab-triggered wet upwellings produce large volumes of melt: Insights into the destruction of the North China craton. *Tectonophysics*. https://doi.org/10.1016/j.tecto.2017.04.009

Youssof, M., Thybo, H., Artemieva, I. M., & Levander, A. (2013). Moho depth and crustal composition in southern Africa. *Tectonophysics*, *609*, 267–287. https://doi.org/10.1016/j.tecto.2013.09.001

Yuan, X. (1996). Velocity structure Fi of the Qinling lithosphere and mushroom cloud model. *Science in China (Series D)*, *39*(1996), 233–244.

Zhai, M.-G., & Santosh, M. (2011). The early Precambrian odyssey of the North China craton: A synoptic overview. *Gondwana Research*, *20*(1), 6–25. https://doi.org/10.1016/j.gr.2011.02.005

Zhang, H. F., Goldstein, S. L., Zhou, X. H., Sun, M., Zheng, J. P., & Cai, Y. (2008). Evolution of subcontinental lithospheric mantle beneath eastern China: Re-Os isotopic evidence from mantle xenoliths in Paleozoic kimberlites and Mesozoic basalts. *Contributions to Mineralogy and Petrology*, *155*(3), 271–293. https://doi.org/10.1007/s00410-007-0241-5

Zhang, S. H., Zhao, Y., Davis, G. A., Ye, H., & Wu, F. (2014). Temporal and spatial variations of Mesozoic magmatism and deformation in the North China craton: Implications for lithospheric thinning and decratonization. *Earth-Science Reviews*, *131*, 49–87. https://doi.org/10.1016/j.earscirev.2013.12.004

Zheng, J. P., O'Reilly, S. Y., Griffin, W. L., Lu, F. X., Zhang, M., & Pearson, N. J. (2001). Relict refractory mantle beneath the eastern North China block: Significance for lithosphere evolution. *Lithos*, *57*(1), 43–66. https://doi.org/10.1016/S0024-4937(00)00073-6

Zhu, G., Jiang, D. Z., Zhang, B. L., & Chen, Y. (2012). Destruction of the eastern North China craton in a backarc setting: Evidence from crustal deformation kinematics. *Gondwana Research*, *22*(1), 86–103. https://doi.org/10.1016/j.gr.2011.08.005

Zhu, G., Niu, M. L., Xie, C. L., & Wang, Y. S. (2010). Sinistral to normal faulting along the tan-Lu fault zone: Evidence for geodynamic switching of the East China continental margin. *Journal of Geology*, *118*(3), 277–293. https://doi.org/10.1086/651540

Zhu, Y., Xu, G., Zhu, H., Zhang, Q. X., & Zheng, T. (2012). Destruction of the North China craton. *Science China Earth Sciences*, *55*(10), 1565–1587. https://doi.org/10.1007/s11430-012-4516-y